THESIS

EVALUATION OF UAS FLIGHT PARAMETERS FOR RAPID MONITORING OF FOREST CHARACTERISTICS

Submitted by

Neal Swayze

Department of Forest and Rangeland Stewardship

In partial fulfillment of the requirements

For the Degree of Master of Science

Colorado State University

Fort Collins, Colorado

Fall 2020

Master's Committee:

Advisor: Wade T. Tinkham

Jody Vogeler
Andrew Hudak

ABSTRACT

EVALUATION OF UAS FLIGHT PARAMETERS FOR RAPID MONITORING OF FOREST CHARACTERISTICS

Forest managers are increasingly turning to finer spatial and temporal resolution data for monitoring forest structure in a rapidly changing world. Traditionally utilized networks of field plots for inventorying forest resources require significant time and financial investments; in response to this, remote sensing techniques have been investigated for providing inventory data across large extents. These methods, including light detection and ranging (LiDAR), require significant financial investment that limits the frequency of repeated surveys. Unmanned Aerial Systems (UAS) have emerged as potential alternatives for generating fine spatial and temporal resolution 2D and 3D data for modeling forest structure. The use of Structure from Motion (SfM) photogrammetry has made it possible to use UAS to collect aerial images and generate point clouds that can be used to model vertical forest structure information in a cost-effective way. Recent research has indicated that UAS-derived SfM point clouds are comparable to LiDAR point clouds for forest structure characterization through both area-based and individual tree observations. However, substantial knowledge gaps exist regarding the influence of UAS flight parameters on SfM-derived forest attributes. This thesis presents two studies to address these knowledge gaps. Specifically, Chapter 1 investigates the influence of UAS altitude and flight speed on modeling aboveground forest biomass through an area-based approach and Chapter 2 evaluates the influence of UAS altitude, camera angle, and flight pattern on extracted tree level and summarized plot and stand level attributes. Results show a strong positive relationship between flight altitude and plot-based aboveground biomass modeling, with UAS predictions increasingly outperforming (2-24% increased variance explained) contemporary LiDAR strategies as acquisition altitude increased from 80-120 m. When monitored at the individual tree level, UAS acquisitions conducted using a combination of crosshatch flight paths and off-nadir camera angles (20-30°) maximized tree detection rates (F-score of 0.77), correlations between stem mapped and extracted tree heights and DBHs (0.995 and 0.910, respectively), and estimates of stand and plot level basal area per hectare and TPH. These results indicate that UAS can be utilized to accurately summarize tree, plot, and stand level forest structure to assist in monitoring and planning of management prescriptions.

ACKNOWLEDGEMENTS

I would first like to thank my advisor Dr. Wade Tinkham, who was beyond helpful and extremely patient throughout the entire design, planning, data collection, processing, and analysis stages of these research projects, and they would not have been possible without his extensive efforts. I would also like to thank my committee members who provided helpful guidance, assistance, and kind support throughout the course of this project: Dr. Jody Vogeler and Dr. Andrew Hudak. I would also like to thank Steven Filippelli with the Natural Resource Ecology Laboratory for his patience, time, expertise, and thoughtful insight into the inner workings of point cloud filtering and analysis, as his assistance has provided a fundamental backbone to all my photogrammetry research.

DEDICATION

I would like to dedicate this thesis to my parents, Sheryl and Gregg Swayze. My parents' push towards remote sensing science from a young age has been pivotal in my development and growth as an emerging researcher in natural resource monitoring. Without their dedicated, unwavering support I would not be here today, and I will be forever grateful for their unconditional love and kindness.

TABLE OF CONTENTS

LIST OF TABLES

LIST OF FIGURES

Chapter 1: INFLUENCE OF UAS FLIGHT ALTITUDE AND SPEED ON ABOVEGROUND BIOMASS PREDICTION

1.1 Introduction

Forests provide a variety of natural and societal benefits, with complex interactions governing recruitment, growth, and mortality processes across multiple-scales (Pan et al., 2013; Anderegg et al., 2015). In order to maximize these benefits, forest managers are increasingly acknowledging the need to monitor and manage forest structure at spatio-temporal scales, which accurately describe the spatial variability in forest dynamics (Briggs et al., 2017). Such forest management decisions require data that represent the continuous nature of ecological phenomena such as structures supportive of wildlife habitat (Vogeler et al., 2016). Complex ecological processes in forests that govern recruitment, growth, and mortality occur at the scale of tree-tree interactions (Dickinson et al., 2016). Traditional forest inventory methods, typically consisting of plot-based networks of *in situ* measurements, are limited in their ability to represent these cross-scale ecological processes and forest spatial arrangements (Lutz, 2015). Despite the need for more continuous methods for characterizing forest structure across landscapes, the acquisition of plot networks of sufficient spatial and temporal resolution is limited by financial constraints (Torresan et al., 2016).

The development of aerial Light Detection and Ranging (LiDAR) techniques for providing spatially continuous observations of forest structure has revolutionized the incorporation of landscape-level information in the decision-making process (Hudak et al., 2009; Nelson, 2013). LiDAR has been shown to produce reliable area-based estimates of forest density (i.e., basal area per hectare; Hudak et al., 2006) and biomass (Bouvier et al., 2015), while also providing reasonable individual tree observations of height and volume (Tinkham et al., 2016). Despite these recent innovations, LiDAR data acquisition can be cost prohibitive as the price of crew mobilization alone starts at >$20,000 (Hummel et al., 2011). This price can preclude low-productivity forest ecosystems from using the technology, as the value of the forest resource must justify the expense of data acquisition for effective management. Smaller land management organizations, which are unable to justify the cost, are commonly prevented from employing these techniques to inform their planning process. Larger organizations that can bear the initial cost may still find it impractical to obtain LiDAR at a temporal resolution suitable for monitoring forests responding to combinations of climatic, disturbance, or management influences (Mitchell et al., 2017). As ecological management drives increased demand for frequent, fine-scale observations of forest structure, new methods of forest structure characterization require further development.

Unmanned Aerial Systems (UAS) are uniquely positioned to meet the demand for fine-scale observations of forest structure by providing spatially-continuous observations at a higher temporal resolution. Professional grade UAS have recently become more accessible to consumers with entry costs under $2,000. Despite the low price point, UAS typically have high-accuracy GPS receivers, automated inertial navigation systems, object detection/avoidance, and improved sensors for very high-resolution (VHR; < 10 cm) remote sensing (Torresan et al., 2017). This combination of technologies is ideal for photogrammetry, which requires high-resolution, spatially-accurate images. Autopilot technology allows users with minimal technical training to operate UAS for repeatable photogrammetry surveys, with commonly used flight planning applications, including PrecisionMapper, Pix4Dcapture, DroneDeploy, DJI Ground

Station Pro, and Altizure. UAS-mounted sensors are starting to surpass the spatial resolution previously only seen in aircraft-based remote sensing, while integrated control and navigation systems are becoming better equipped to maximize the sensor's potential. Preliminary studies have evaluated both fixed-wing and multirotor UAS platforms equipped with a range of sensors for data collection, including consumer and professional grade RGB compact camera systems, among others (Wallace et al., 2016; Fritz et al., 2013; Zarco-Tejada et al., 2014; Webster et al., 2018; Thiel & Schmullius, 2016). The high-cost and temporal resolution limitations of LiDAR are where UAS can fill data needs for forest management organizations; UAS cost orders of magnitude less than aircraft-based LiDAR acquisitions and can be flown as often as favorable conditions are met. Despite their potential, UAS are currently limited in the area that can be covered in a single acquisition by relatively short flight times due to battery capacity and governmental regulations requiring pilots to maintain a line of sight or visual contact with the platform at all times. Additionally, UAS are known to be impacted by changing light conditions during acquisition (O'Connor et al., 2017) and high winds, which can lead to errors in image matching (Iglhaut et al., 2019). While UAS have limitations, the low cost of deployment and the ability to collect VHR data demonstrates a niche for more frequent monitoring at the stand-scale that UAS can provide.

Over the last decade, numerous studies have utilized UAS to generate VHR two-dimensional orthomosaic maps (Torrez-Sanchez et al., 2015; Fraser & Congalton, 2018) and three-dimensional point clouds of forest structure and terrain using various Structure from Motion (SfM) processing algorithms (Thiel & Schmullius, 2016; Frey et al., 2018). SfM algorithms identify common points within overlapping images and, through a geometric process utilizing the position and rotation of captured images, a three-dimensional point cloud is generated (Frey et al., 2018). Due to the high degree of overlap, SfM point clouds can have data densities in excess of 1,000 points m^{-2} compared to LiDAR's common 4-30 points m^{-2}, and therefore have the potential to better capture the fine-scale complexity of forest structure than LiDAR. Additionally, recent studies have found that including UAS orthomosaic spectral data in SfM modeling resulted in it being a significant parameter in 80% of models predicting forest biomass (Domingo et al., 2019).

Early UAS research has revealed that the accuracy of forest structure estimates varies based on data acquisition parameters such as forward and side image overlap, flight altitude, and speed (Dandois et al., 2015, Seifert et al., 2019, Frey et al., 2018). Dandois et al. (2015) demonstrated that increasing the levels of forward and side overlap until at least 80% led to improved location and height accuracies in forested environments. When controlling forward and side overlap separately, Seifert et al. (2019) found that maintaining high (>90%) forward overlap with lower side overlap (~70%) provided a balance between data accuracy, flight time, area coverage, and data processing time. These studies have concluded that forward overlap should be maximized as it does not impact flight time or the area covered in a single acquisition. In contrast, side overlap can be reduced depending on data objectives to achieve a larger acquisition area.

Several studies have evaluated the influence of flight altitude on data quality and forest structure characterization accuracy with conflicting results. Seifert et al. (2019) found that low altitude flights within 15-20 m of the vegetation canopy resulted in significantly more image registration points with improved precision. However, Fraser & Congalton (2018) found that flying at 100 m above the vegetation canopy provided the best image alignment. Additionally, Torres-Sánchez et al. (2015) found no significant impact of altitude on object-based canopy parameter extraction. Faced with these conflicting results, it is necessary to standardize flight acquisition parameters for a consistent interpretation of UAS survey results across different environments and methods. Additionally, each of these studies evaluated how altitude impacted image alignment for study areas at similar forests to understand the role of forest structure characterization on end-product forest measurements.

While these results indicate a range of optimal parameters for UAS image alignment within different vegetation types, significant knowledge gaps exist for both guiding future image acquisition and the translation of parameter optimization to the accuracy of UAS-based forest structure characterization. There is, therefore, a significant need for systematic testing of flight survey parameters in order to quantify the impact of forest structure on SfM-derived point clouds (Torres-Sánchez et al., 2015).

This study seeks to examine how flight altitude and speed impact UAS model reliability in explaining forest biomass compared to standard aerial LiDAR modeling strategies across a range of forest structures found in ponderosa pine (*Pinus ponderosa var. scopulorum* Dougl. Ex Laws.) dominated forests. Specifically, comparisons of variance explained, and precision between UAS- and LiDAR-based models of forest biomass will be examined through their response to flight altitude and speed. Additionally, this analysis will investigate how segmentation of SfM point clouds based on spectral indices impacts model performance. The effects of flight altitude and speed will be discussed in terms of data collection, processing times, and data density.

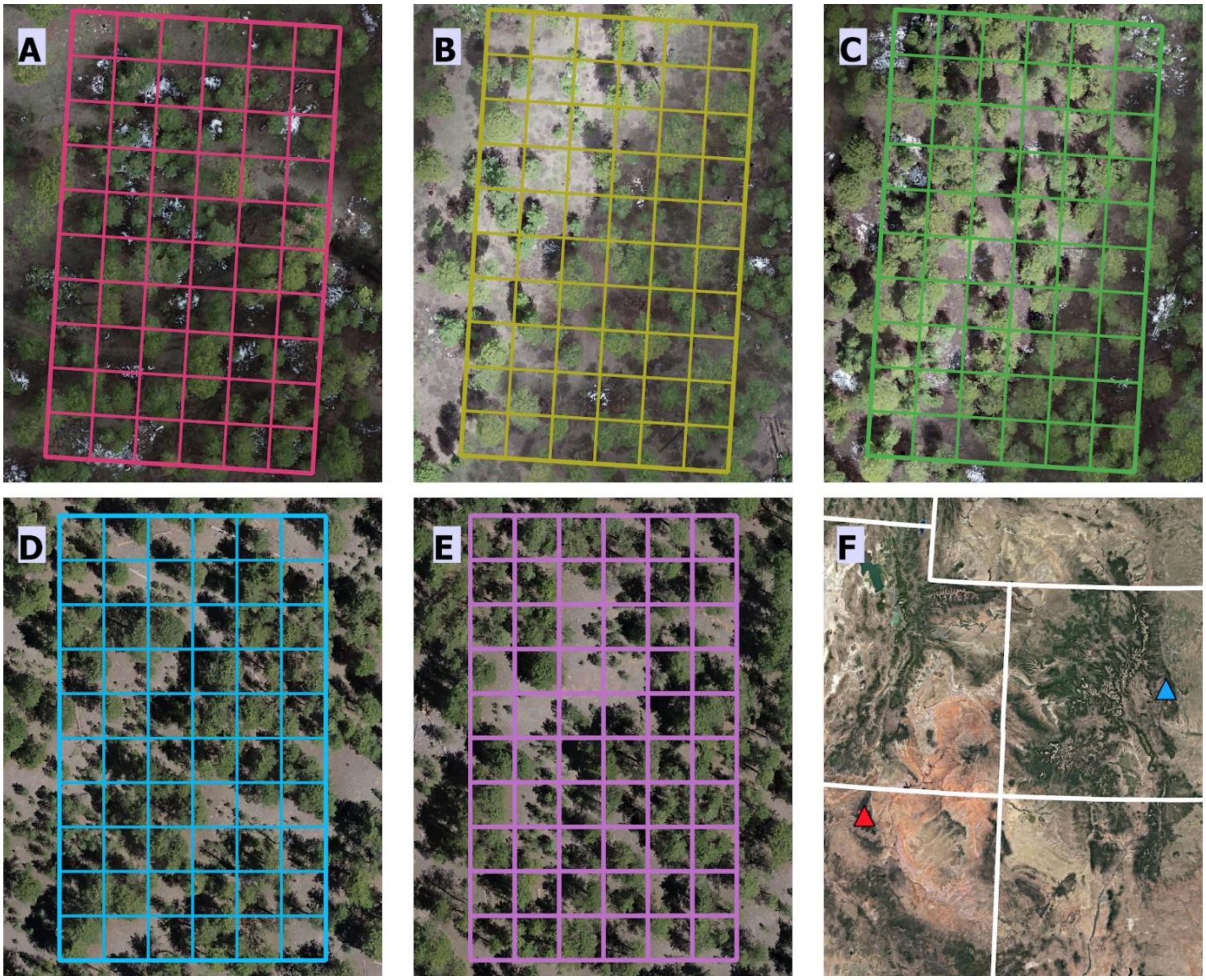

Figure 1.1. Five 60 x 100 m study areas at the Kaibab National Forest in Northern Arizona (KNF1: A, KNF2: B, KNF3: C) and Manitou Experimental Forest in Central Colorado (MEF1: D, MEF2: E), with the location of KNF study area (red) and MEF study area (blue) displayed in panel F.

1.2 Methods

1.2.1 Study Area and Field Data

This study was conducted across two ponderosa pine dominated forests with existing aerial LiDAR and stem mapped forest inventories in the central Rocky Mountains (Figure 1.1). Within these forested areas, five study units were selected to represent a range of forest densities. The first forest is the N1 forest dynamics site located within the Manitou Experimental Forest on the Pike-San Isabel National Forest in Colorado, about 40 km northwest of Colorado Springs. The average elevation is 2,500 m, with a mild slope (< 5%) to the southeast. This location provides an example of a typical human-influenced montane ponderosa pine forest, as it was selectively logged between 1880 and 1886 (Boyden et al., 2005). After logging, the forest was undisturbed with no significant fire since 1846 and only minor mountain pine beetle disturbance in the late 1970's. During the 140 years following harvest activities, the N1 forest has since experienced several regeneration pulses that have led to varying forest densities, with minor components of Douglas-fir (*Pseudotsuga menziesii* (Mirb.) Franco var. *glauca* (Beissn.) Franco) and blue spruce (*Picea pungens* Engelm.) in the understory. Native grasses and a few low growing woody shrubs comprise the sparse understory vegetation. To control for variation in forest densities during testing, the N1 forest was divided into two separate study units for UAS data acquisition, hereafter referred to as MEF1 and MEF2 (Table 1.1).

Table 1.1. Forest stand structure at the Manitou Experimental Forest (MEF) and Kaibab National Forest (KNF) study units, reported as mean (standard deviation) of 0.01 ha sampling unit.

Study Area	QMD (cm)	Max Tree Height (m)	Basal Area (m^2 ha^{-1})	Trees ha^{-1}	AGB* (tons ha^{-1})
KNF1	30.3 (14.8)	15.9 (8.0)	26.9 (22.0)	300 (197)	90.6 (51.1)
KNF2	31.2 (22.0)	14.9 (9.6)	21.2 (22.1)	200 (186)	80.7 (55.6)
KNF3	32.9 (14.6)	22.2 (6.2)	44.5 (29.2)	626 (446)	128.9 (54.7)
MEF1	21.7 (11.8)	17.5 (6.6)	24.8 (15.9)	931 (806)	90.2 (34.9)
MEF2	23.5 (11.3)	17.1 (5.4)	26.9 (17.4)	701 (407)	93.4 (35.1)

* aboveground biomass calculated using Jenkins et al., 2003

The Lookout Canyon forest dynamics site is located in the Kaibab National Forest in northern Arizona, approximately 65 km southeast of Kanab, Utah, at an elevation of approximately 2,400 m. The forest is primarily composed of ponderosa pine and was divided into three 4-hectare stands for thinning, including a control stand and two stands thinned to 9.2 and 13.8 m^2 ha^{-1} of basal area in 1993 (Table 1.1), hereafter KNF1, KNF2, and KNF3. Following thinning, quaking aspen (*Populus tremuloides* Michx.) began reestablishing within the understory alongside considerable pulses of ponderosa pine regeneration. A prescribed fire in an adjacent stand escaped in 1999 and burnt through the understory killing more than 600 small diameter trees.

All trees taller than 1.37 m were stem mapped at each of the five study units using a grid of known survey locations. For each mapped tree, the species, diameter at breast height (1.37 m; DBH), and height was recorded. Stem mapping of the 60 x 100 m study units (0.6 ha) was completed in July 2018 for MEF1 and MEF2 and in May 2019 for KNF1, KNF2, and KNF3. The study stem maps were divided into 10 x 10 m (0.01 ha; n = 60) sampling units. Each sampling unit was analyzed separately in the Central Rockies variant (Keyser & Dixon, 2008) of the Forest Vegetation Simulator (Dixon, 2002) to determine total aboveground biomass (AGB). Biomass was estimated as metric tons ha^{-1} using allometries from Jenkins et al. (2003) as implemented in the Forest Vegetation Simulator.

1.2.2 UAS Data Acquisition

UAS image data was collected using a DJI Phantom 4 Pro (Dá-Jiang Innovations Science and Technology Co. Ltd., Shenzhen, China) multirotor equipped with a 20-megapixel (5472 x 3648 pixels) metal oxide semiconductor (CMOS) red-green-blue (RGB) sensor, with a fixed 8.8 mm focal length (Figure 1.2A). For all image acquisitions, the camera was set to infinity focus, with an aperture (F-stop) of 5.6, a shutter speed of 1/500s, and ISO values ranging from 100 to

200 depending on lighting conditions. The aircraft recorded geolocation (x, y, and z) and camera parameter values for each captured photo to a manufacturer-stated vertical accuracy of ±0.5 m and horizontal accuracy of ±1.5 m (https://www.dji.com/phantom-4-pro).

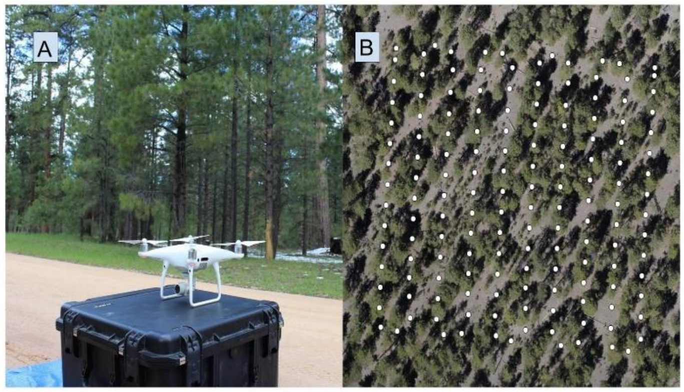

Figure 1.2. (A) DJI Phantom 4 Pro aircraft at KNF study area. (B) Conventional UAS survey depicting the automated route generated by Altizure. The white circles represent approximate camera capture locations for a flight 120 m above ground level.

Flight planning and execution were performed using Altizure version 4.6.8.193 (Shenzhen, China) for Apple iOS. The application was utilized to pre-program automated UAS flight paths with desired altitude, forward and side photo overlap, flight speed, exposure, aperture and shutter speed (Figure 1.2B). To better understand the optimal altitude for generating photogrammetric models of forest structure, 40 independent UAS flights were planned (8 acquisitions per study area) at randomly chosen altitudes ranging from 40 to 120 m above ground level. Three flight speeds were systematically assigned to each altitude, including 2, 3, and 4 m sec^{-1}. This study utilized a nadir camera angle, with 90% forward and 90% side photo overlap for all data acquisitions. This overlap combination was selected based on previous research that suggested that forward and side overlaps greater than 80% improved image alignment, improved tree height estimation, and reduced understory occlusion in UAS surveys (Dandois et al., 2015; Frey et al., 2018).

An adaptive flight boundary methodology was used to maintain a constant number of flight lines and photo density or the number of photos viewing the same location at each of the desired altitudes. Initial testing showed that failing to increase flight boundary dimensions as altitude increases led to fewer flight lines and photos, resulting in reduced data density for the point cloud generation. In order to implement this methodology, 10% of the camera footprint (widths and lengths in meters) was determined across different altitudes and multiplied by 10 to ensure maximum photo density at the center of the study area. This resulted in flight boundaries varying between 80 x 110 m and 161 x 110 m at flight altitudes of 40 and 120 m, respectively. At the Kaibab study units, it was determined that three of the randomly assigned UAS surveys could not be completed due to concerns of collision with the canopy at the lowest altitudes (<45 m), resulting in a total of 37 flights.

All UAS surveys were flown between April and August 2019 and within three hours of solar noon to maintain a minimum solar angle of 50° from the horizon. All flights were conducted within the line of sight of the remote pilot in command with the assistance of a visual observer to comply with Part 107 Federal Aviation Administration regulations.

1.2.3 Ground Control Points

The methodology for ground control point (GCP) implementation followed the procedures outlined in the Australian Photogrammetry for Forest Inventory Planning Guide (Osborn et al., 2017). Ten high visibility ~0.2 m^2 GCPs were collected using a Trimble GeoXT (Trimble Inc., Sunnyvale, CA, USA) with SBAS real-time corrections for each of the five study units with accuracies of <1 m. All points were placed to account for visibility from the air with the UAS. Four points were set as close to each corner as possible, one along each long edge and the remaining four points were distributed throughout the center (Figure 1.2). The GCPs were differentially corrected using Trimble Pathfinder Office software. GCPs were imported into ArcGIS 10.6.1 (ESRI Inc.; Redlands, CA, U.S.A.), and projection was defined as the WGS 1984 coordinate system to match the UAS imagery. Latitude, longitude, and altitude were then exported for use in georectifying the UAS imagery.

1.2.4 UAS Structure from Motion Point Cloud Generation Data Processing

Agisoft Metashape version 1.5.3 (www.agisoft.com; Agisoft LLC, St. Petersburg, Russia) was used to implement a SfM photogrammetry algorithm. SfM algorithms generate 3D point clouds by identifying image features and GCPs in each image and using these features to align the images in space. After these matches are found, a photogrammetric sparse bundle adjustment calculates the 3D location of each of the images in space using the camera parameters and the 3D geometry of the objects found within the images (Dandois et al., 2015). The Agisoft Metashape processing was implemented through a cloud server utilizing a 2.7 Ghz Intel Xeon E5 2686 V4 computer processor unit with two NVIDIA Tesla M60 graphics cards, and a total of 240 gigabytes of random-access memory.

The Agisoft Metashape workflow closely followed the processing methodology found in the Agisoft Photoscan user manual (Link, 2017), with the only departure including local testing of the dense cloud and depth filter settings. Using the MEF1 95 m acquisition, the 20 possible combinations of the Agisoft Metashape build dense cloud quality settings and depth filtering settings were tested on this photo dataset, resulting in 20 unique point clouds with different point cloud densities and processing times. From this it was determined that SfM setting in Agisoft Metashape for forest reconstruction in this study would be set to High quality and Mild depth filtering as these settings provided a balance between data density and processing time and align with settings commonly used in other studies (Fraser & Congalton, 2018; Goldbergs et al., 2018). The full suite of selected Agisoft Metashape settings for image dataset processing is depicted in Appendix Table 1.1.

Each of the SfM point clouds were exported from Agisoft Metashape with UTM Zone 13N and 12N projections for Colorado and Arizona, respectively. CloudCompare version 2.10.1 (www.cloudcompare.org), a software designed for 3-dimensional point data comparison, was used to visually inspect each point cloud to ensure complete dense cloud reconstruction. Agisoft Metashape processing reports were also generated and checked to ensure similar processing errors across the point cloud models. Clouds with significant processing errors or incomplete reconstruction were reprocessed to ensure comparable accuracy and quality across the 37 surveys.

1.2.5 LiDAR Datasets

At the Manitou Experimental Forest sites aerial LiDAR data was acquired in August 2014 at a nominal point density of 5.74 points m^{-2}. Aerial LiDAR data for the Kaibab National Forest sites was acquired in the winter of 2012 at a nominal point density of 13.70 points m^{-2}. The time difference between the LiDAR acquisitions and the field inventory corresponds to average tree height growths of 0.5 m at MEF and 1.1 m at KNF, derived from prior site inventories. The LiDAR point clouds were cropped to the five study unit extents and used as an industry standard for comparing the accuracy of the UAS modeled forest biomass.

1.2.6 Point Cloud Processing

All 37 SfM UAS point clouds and the five aerial LiDAR point clouds were processed using LAStools version 1.2 (http://lastools.org). The LiDAR and SfM point clouds were initially clipped to a buffered extent of 90 m x 130 m to provide a margin around each of the five study areas and to prevent geometry irregularities known to occur at the edge of point clouds during processing. Point clouds were filtered to remove noise by selecting block minimum points and fitting a digital elevation model with a spline fit; points that fell below the digital elevation model were classified as noise and removed from further processing. The remaining points were classified as either ground or non-ground points.

After filtering and classification, each point cloud was clipped to the final 60 x 100 m study unit extent. Points classified as ground were extracted from each point cloud and visually compared to the LiDAR ground points in CloudCompare, revealing a slight Z-axis misalignment between the SfM and LiDAR datasets. This misalignment is attributed to low vertical precision in the GCPs from overstory trees, causing some degree of GPS satellite signal occlusion. There was minimal observed x- and y-axis misalignment between the SfM and LiDAR ground points, which suggested that the GCPs had high horizontal precision. This SfM ground point cloud misalignment was corrected using the iterative closest point - fine alignment tool to develop a custom transformation matrix for each SfM point cloud that was applied to the full SfM point cloud to align it with the LiDAR point cloud. Following geometric transformation, each SfM and LiDAR point cloud was height normalized against their classified ground points.

The SfM points clouds were further processed to investigate how segmentation of the points based on spectral indices impacts the prediction of forest biomass. To train the point segmentation, all filtered and classified point clouds at a study site were merged using LAStools and loaded into CloudCompare. From the merged point cloud, 15 random samples each of canopy and stem (each containing 20,000-60,000 points) were manually extracted to ensure pure representation of both stem and canopy points. These classified stem and canopy point samples were imported to the R statistical programming language (R core Team, 2019) using the lidR package (Roussel & Auty, 2019). From each point sample, the red and green reflectance data was used to calculate the Normalized Green-Red Ratio (NGRR) using Equation 1.

$$NGRR = \frac{G_{band} - R_{band}}{G_{band} + R_{band}} \qquad \text{[Equation 1]}$$

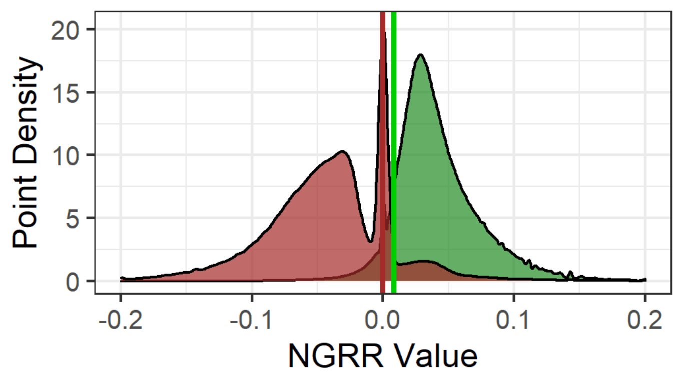

Figure 1.3. Example density plot of the canopy (green) and stem (red) NGRR values sampled from SfM point clouds at the MEF1 study area, where overlapping distribution segments are brown. Red and green vertical lines represent the 90th and 10th percentile of the stem and canopy values, respectively.

Visual inspection of density plots for the stem and canopy indexed points for each study site (Figure 1.3) showed segregation of NGRR values when the data was split with stem values less than their 90th percentile and canopy values greater than their 10th percentile. Across the five study units, the stem 90th percentile varied from -0.0096 to 0, and the canopy 10th percentile varied from 0 to 0.0747. These segmentation thresholds were used to segment the

SfM point clouds into three different categories for each of the 37 acquisitions: Stem, Canopy, and Standard, where Standard is the non-NGRR classified point cloud (Figure 1.4).

1.2.7 Forest Biomass Modeling

To develop models of aboveground biomass the three SfM point clouds for each of the 37 UAS acquisitions and the five LiDAR point clouds were processed using the lascanopy utility in LAStools. This function generated 21 point cloud distributional metrics for each of the 60 sampling units (Figure 1.1) that aligned with the FVS modeled AGB for each study unit. These distributional metrics included maximum, average, minimum, standard deviation of height, skewness, kurtosis, average square height, percentiles (5, 25, 50, 75, 90), bicentiles (5, 25, 50, 75, 90), vertical complexity index (0, 1, 2), and percent canopy cover.

At each site, the LiDAR point cloud distribution metrics were used to create baseline predictions of AGB using the randomForest package (Liaw and Wiener, 2002) of the R statistical programming language. In order to refine the number of predictors being used to model AGB, the Random Forest Model Selection tool (Murphy et al., 2010) was used to select the top five predictors in each model. The top five point cloud metrics for each dataset were used as predictor variables to model AGB using a series of random forest regressions with 10,000 trees each (Breiman, 2001), where the 60 sampling units were randomly divided into training observations (80% or n=48) and validation observations (20% or n=12). The same process for modeling AGB was repeated for each UAS data acquisition using the Standard SfM point cloud distribution metrics and then again with the point cloud distribution metrics combined for the Standard, Stem, and Canopy datasets, referred to as Standard + NGRR hereafter. In total, 74

UAS random forest models (37 Standard SfM and 37 Standard + NGRR SfM) were compared against the five LiDAR random forest models for the same respective study unit.

Figure 1.4. Example point clouds and density histograms for high biomass (top panels) and low biomass locations (bottom panels), including LiDAR (A and E), Standard SfM (B and F), Stem SfM (C and G), and Canopy SfM (D and H).

1.2.8 Model Evaluation

The 74 SfM random forest models were evaluated by relativizing them against their respective LiDAR random forest model through the calculation of percent change in model performance metrics of the Coefficient of Determination (ΔR^2; Equation 2), Root Mean Squared Error (ΔRMSE; Equation 3), and Mean Absolute Error (ΔMAE; Equation 4).

$$\Delta R^2 = \frac{SfM\ R_{ij}^2 - LiDAR\ R_i^2}{LiDAR\ R_i^2} \times 100 \qquad \text{Equation 2}$$

$$\Delta RMSE = \frac{SfM\ RMSE_{ij} - LiDAR\ RMSE_i}{LiDAR\ RMSE_i} \times 100 \qquad \text{Equation 3}$$

$$\Delta MAE = \frac{SfM\ MAE_{ij} - LiDAR\ MAE_i}{LiDAR\ MAE_i} \times 100 \qquad \text{Equation 4}$$

Where i denotes an individual study site, while j signifies the individual UAS acquisitions within that site. These relativized metrics should be interpreted as positive values of ΔR^2 indicating percentage improvement of the UAS model over the LiDAR model, while negative values of ΔRMSE and ΔMAE indicate percentage reductions in the UAS model compared to the LiDAR model. To standardize the effect of altitude on model performance across the five sites, the effect of altitude was also evaluated as a ratio ($A{:}L_H$; Equation 5) of altitude (A) compared to Lorey's Mean Height (L_H; Equation 6).

$$A: L_H = \frac{Altitude\ (m)}{L_H(m)} \qquad \text{Equation 5}$$

$$L_H = \frac{\sum g \times h}{\sum g} \qquad \text{Equation 6}$$

Where g is a tree's basal area (m^2) and h is a tree's height (m), meaning that L_H can be interpreted as the weighted height of the forest were a stand with more regeneration will see this value be less than the arithmetic mean. The model performance metrics ΔR^2, ΔRMSE, and ΔMAE were all evaluated as a function of altitude and L_H.

To evaluate the relationship between Standard UAS random forest model performance metrics with UAS data acquisition flight altitude and speed, linear mixed-effects regression was performed. In this analysis, the 37 combinations of UAS acquisition altitude and speed were treated as fixed effects, while the five study sites were treated as a random-effect. Additional covariates of stand-level forest structure and AGB were also evaluated for their influence on model performance. While testing for interactions, a stepwise procedure was used to identify the best subset of explanatory factors that minimized the Akaike Information Criterion (AIC). All regression was performed using lme4 packages (Bates et al., 2015) of the R statistical programming language.

Finally, after pooling the important point cloud distribution metrics from each random forest model, they were evaluated based on the proportion of models they appeared in. This analysis was extended to contrast the changes in important distribution metrics for the Standard SfM models with the Standard + NGRR SfM models.

1.3 Results

1.3.1 LiDAR AGB Model Performance

The five aerial LiDAR random forest model results for AGB varied across the study sites, with R^2 averaging 0.539 (range 0.424 - 0.666). However, R^2 values for the three MEF study sites were 0.129 higher than those for the two KNF study sites. Additionally, the KNF study sites had nearly twice as much variation in the 0.01 ha sampling units for AGB, basal area ha^{-1}, and max tree heights compared to the MEF sites (Table 1.1). Similar contrasts in model performance were found in RMSE, which ranged from 23.9 to 56.8 tons ha^{-1}, and MAE, which ranged from 15.8 to 55.1 tons per ha^{-1}. Variation in these metrics across the five study sites followed the same trend as the R^2 values.

1.3.2 Standard AGB Model Performance

Random forest AGB model performance for Standard UAS SfM parameters compared to LiDAR models of AGB varied across flight altitudes (Figure 1.5). The lowest altitude UAS acquisitions at each study site failed to reconstruct the vertical profile of the vegetation and provided substantially worse results compared to the LiDAR predictions (average ΔR^2 = -20.6%). For acquisitions that correctly generated SfM point clouds, the average ΔR^2 was 4.4%, with model performance generally improving with increased altitude. Linear mixed-effects modeling of ΔR^2 as a function of flight altitude and speed demonstrated a significant effect of flight

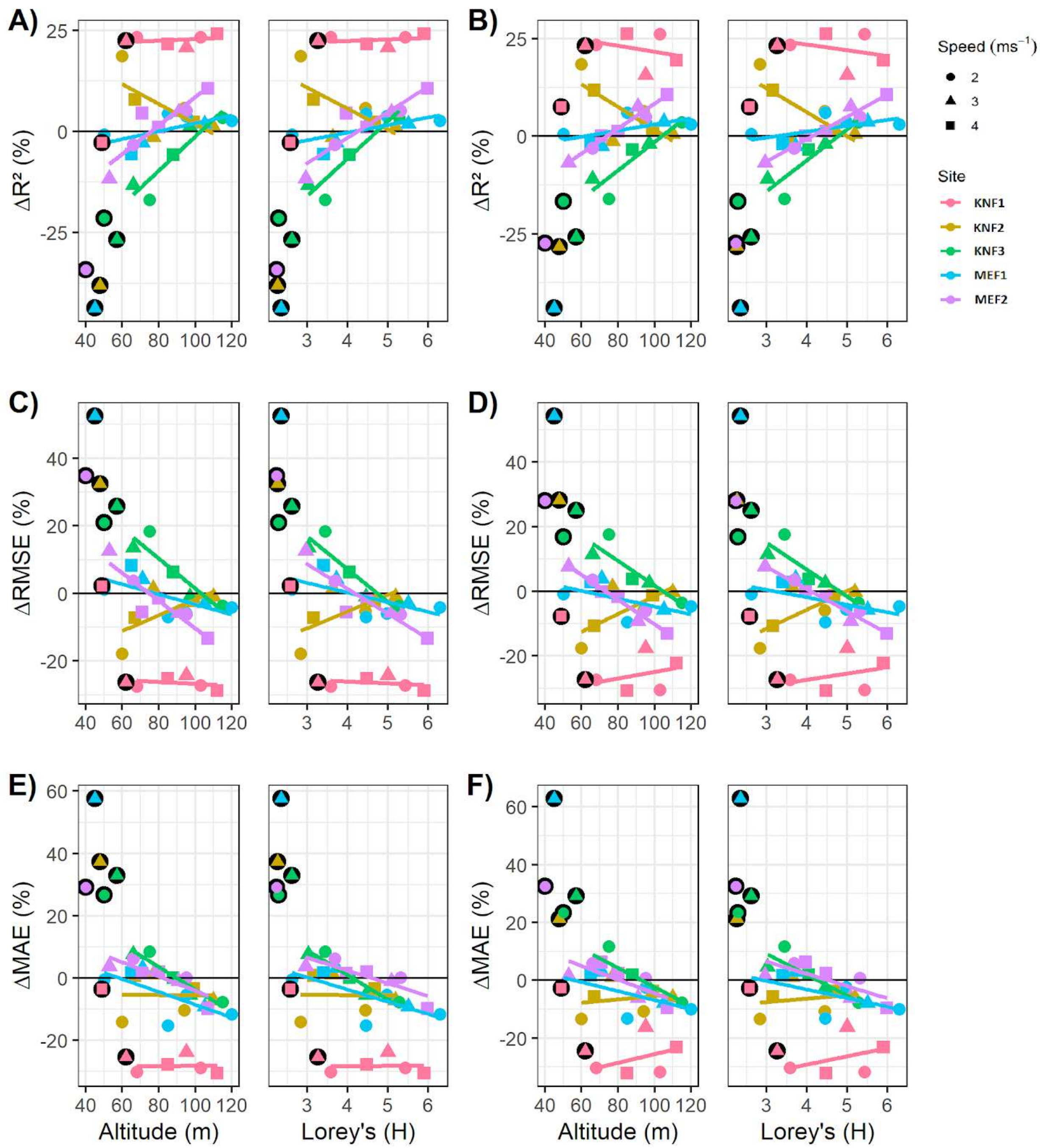

Figure 1.5. Comparison of Standard (panels A, C, & E) and Standard + NGRR (panels B, D, & F) AGB model performance metrics relativized to LiDAR, including percent ΔR^2 (panels A & B), ΔRMSE (C & D), and ΔMAE (E & F). The panel is split to show the influence of altitude above ground (left) and the ratio $A:L_H$ (right). Points in black circles represent acquisitions that failed to reconstruct the forest canopy.

altitude on ΔR^2, but not flight speed (Table 1.2). Average ΔR^2 varied from nearly a 20% reduction in prediction performance at the lowest altitudes to nearly a 20% improvement in prediction performance over the LiDAR models at the highest altitudes (Figure 1.6). Similar improvements with increased altitude were seen for Standard UAS SfM models of AGB for ΔRMSE and ΔMAE (Figure 1.5). For models correctly generating SfM point clouds, the ΔRMSE and ΔMAE were reduced by 5.1% and 6.9%, respectively.

Table 1.2. Linear mixed-effects model of the influence of flight altitude and speed on change in aboveground biomass model R^2. The five study sites were treated as a random effect.

Parameter	Coefficient	Standard Error	t-value	p-value
Standard Flight Altitude				
Intercept	-30.272	10.401	-2.910	0.0067
Altitude (m)	0.403	0.082	4.908	<0.001
Speed (m s^{-2})	-0.574	2.325	-0.247	0.8068
Relativized Flight Altitude				
Intercept	-30.403	10.134	-3.000	0.0053
Lorey's Height	7.996	1.594	5.018	<0.001
Speed (m s^{-2})	-0.606	2.316	-0.261	0.7955

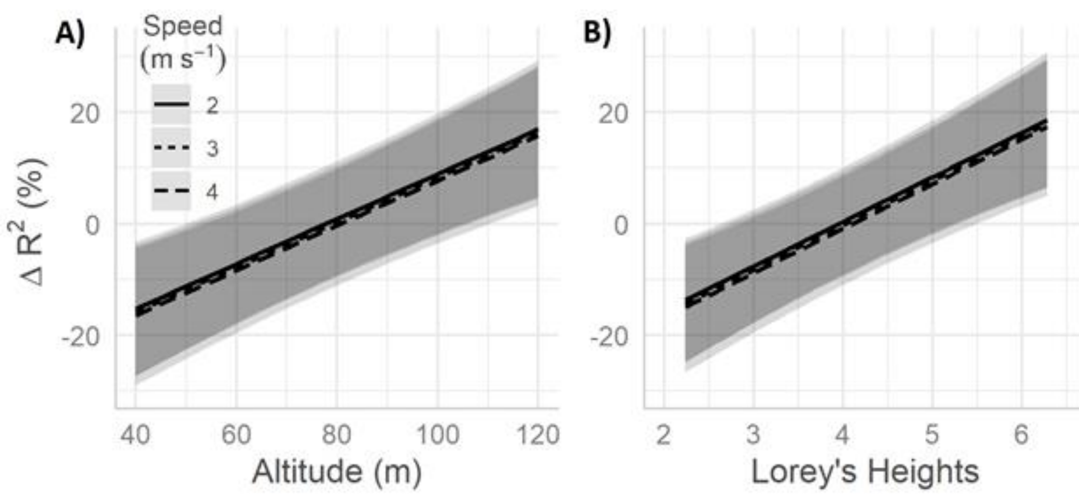

Figure 1.6. Linear mixed-effects model results for the 37 Standard SfM AGB models.

Standard UAS SfM parameters always resulted in improved model performance at the highest altitudes, with altitudes at which models began outperforming LiDAR models varying from ~80 to 100 m (Figure 1.5). Standardizing flight altitude as a ratio of altitude divided by Lorey's Height tightens this threshold for outperforming the LiDAR models to 4-4.5 times the site's Lorey's Height. Similar to flight altitude, Lorey's Height significantly explains the variation in ΔR^2 (Table 1.2). The linear mixed-effects model indicates that for every Lorey's Height that acquisition altitude increases there is an ~8% improvement in ΔR^2, indicating that at four times Lorey's Height UAS SfM modeling of AGB typically exceeds the performance of aerial LiDAR models in ponderosa pine dominated systems (Figure 1.6).

1.3.3 Standard + NGRR AGB Model Performance

Integration of Standard + NGRR UAS SfM parameters for AGB modeling provided a 6.0% average increase in ΔR^2 across all flights compared to the modeling only using the Standard SfM parameters (Figure 1.5). This increase was found to be significant (p-value = 0.0181) when tested with a paired Wilcoxon signed rank test. Although there was not a significant difference (p-value = 0.5453) in the ΔMAE, the Standard + NGRR models did significantly (p-value = 0.0284) decrease ΔRMSE by 6.5% compared to models only using the Standard SfM parameters. Linear mixed-effects model coefficients for the Standard + NGRR SfM models revealed no significant differences compared to the Standard SfM linear mixed-effects models.

1.3.4 AGB Model Variable Importance

For the Standard SfM models of AGB the five most important variables fluctuated across models, but seven variables stood out from the rest and showed up in at least 40% of these models (Figure 1.7A). Across all flight altitudes and sites, the average height of points above ground showed up in 74% of all models (or 27 of 37 models) and was the highest ranked variable in nearly 40%. The remaining six variables that were highly selected varied in being in 43 to 57% of models, with their importance metrics level fluctuating. These seven metrics accounted for 73.7% of all metrics selected in the Standard SfM models.

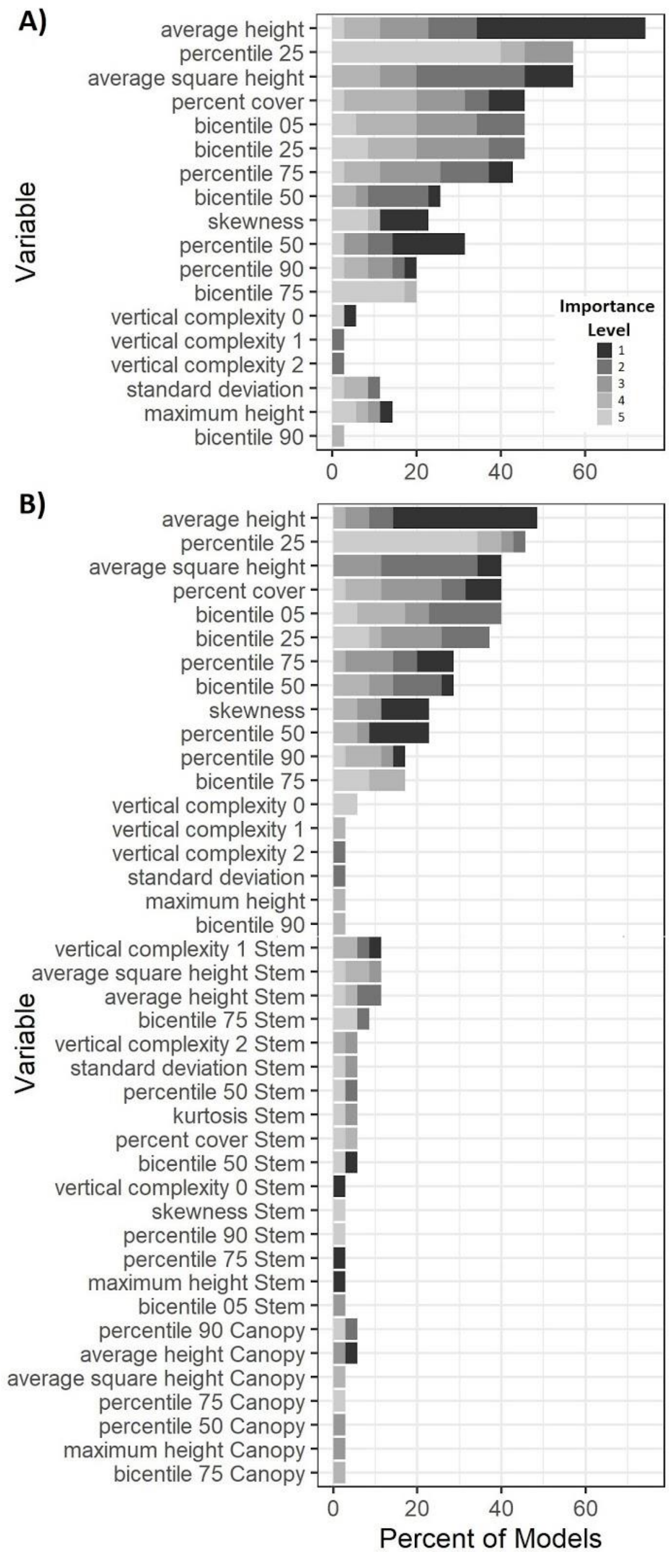

Figure 1.7. Random forest variable importance for Standard (A) and Standard + NGRR (B), values are sorted based on the percentage of the 37 models they appeared in for each grouping.

The top seven variables from the Standard metrics did not change even after including the NGRR segmented point cloud metrics (Figure 1.7B). However, these seven metrics only accounted for 56% of all selected metrics when the Standard and NGRR metrics were considered. This reduction was due to 17.8 and 4.9% of all selected variables being chosen from the Stem and Canopy distributional metrics, respectively. Of these NGRR metrics, only Stem average height, average squared height, and vertical complexity 1 were important in more than 10% of models (Figure 1.7B). Additionally, none of the Canopy distributional metrics occurred in more than 2 of the 37 models.

1.4 Discussion

1.4.1 AGB Model Performance

This study evaluated the impact of flight altitude and speed on UAS SfM plot-based modeling of aboveground biomass, with UAS modeling outperforming LiDAR at higher altitudes. Across all sites, UAS acquisitions above 80 m AGL resulted in improved model performance compared to aerial LiDAR; above this altitude relative to LiDAR models R^2 increased on average by 7.4% and RMSE and MAE were decreased by 8.8 and 10.9%, respectively (Figure 1.5). While the authors could not identify other studies that have seen this relationship for UAS biomass modeling, inference might be drawn from studies looking at relationships between UAS SfM reconstruction quality and flight altitude. Fraser and Congalton (2018) tested the effect of flight altitude on image alignment and found that flying at their highest tested altitude provided the best results. Other studies have not directly seen an influence of altitude on SfM vegetation reconstruction, but still concluded that flying higher provided the benefit of greater acquisition extents (Torres-Sanchez et al., 2015). This literature connects the small decrease in image resolution at higher altitudes with improved imaging matching by reducing the influence of vegetation movement in the wind (Iglhaut et al., 2019). There is reason to believe this improved image matching better represents vegetation vertical distributions and improves AGB modeling at the plot-level. However, there is reason to believe that continued increasing of flight altitude and decreasing of image resolution will at some point result in decreased performance in modeling forest attributes like AGB.

While generally flying higher provided better model results, flying at altitudes too close to vegetation posed significant problems. Photogrammetric reconstruction of treetops was incomplete for the lowest altitudes tested at each site due to the proximity of the onboard UAS camera to the treetops. Failure to reconstruct the tops of trees led to inaccurate point cloud distributional metrics and resulted in poor AGB biomass model performance in our study (Figure 1.8). This truncation at the top of the point cloud can be seen in Figure 1.8, where the worse models represent low altitude flights that failed to reconstruct the tops of trees. The dependency of reconstruction on altitude is attributed to the proximity of treetops to the sensor, when the vegetation is too close, there is not sufficient photo overlap at the top of the tree compared to the programmed 90% forward and 90% side overlaps at the ground surface. While it varied across sites, consistent point cloud generation was achieved for all flights above 65 m altitude or ~1.9 times the maximum tree height within a given site. While lower altitude UAS acquisitions can provide greater resolution, studies that require close proximity acquisition of forest canopies should consider increasing the photo overlap to compensate for the depth of vegetation. Therefore, as the height of vegetation increases, the flight altitude needed to reconstruct forest canopies should increase as well.

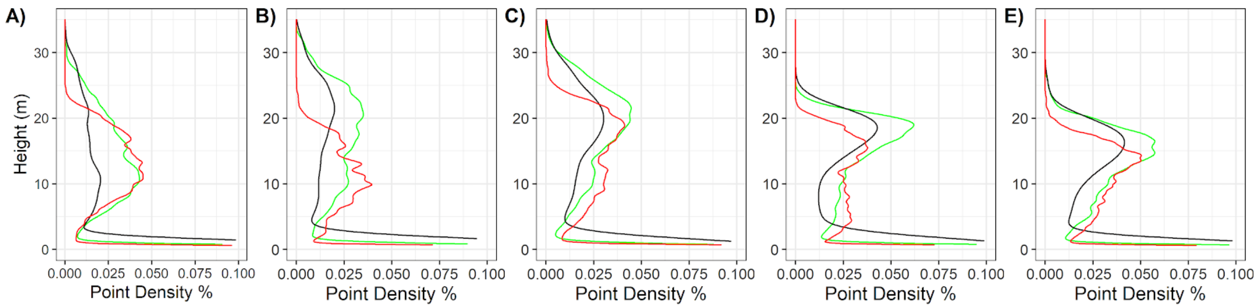

Figure 1.8. Relative point density as a function of height above ground for the best and worst Standard SfM AGB models (green and red respectively) at each site (from left to right KNF1, KNF2, KNF3, MEF1, and MEF2), with LiDAR point cloud distributions displayed in black.

Standardizing altitude as a ratio of Lorey's Height for each flight provided better consistency for interpreting the relationship between UAS flight altitude and vegetation height. All flights above four times a site's Lorey's Height resulted in improved model performance, with an average increase of 7.8% for R^2 and decreases of 9.3 and 11.6% for RMSE and MAE, respectively (Figure 1.5). Currently, it is difficult to evaluate the effects of altitude in different vegetation types, as it has not become common practice to report vegetation height or its relationship to flight altitude. Standardization of this is necessary within the UAS literature to improve cross-study synthesis of results. While flying above four times a site's Lorey's Height promotes improved AGB modeling within these forest systems, understanding the transference of this to forest systems that can reach dominant tree heights in excess of 40 m need investigation. Such work within the United States will need to address FAA regulations limiting UAVs to 120 m AGL flight altitudes.

Our results did not find a statistically significant effect of flight speed on resultant AGB models (Table 1.2), which could be attributed to the narrow range of relatively slow flight speeds (2-4 m sec^{-1}) evaluated. These findings differ from O'Connor et al. (2017), which found that increased flight speed causes image blurring, location errors, and, therefore, increased image alignment errors. While there is reason to believe this should propagate through to the modeling of forest attributes like AGB, it does not appear the moderate increases in flight speed tested in this study detrimentally impacted UAS SfM plot-based biomass modeling. Although not significant in this study, flight speed should remain an important consideration in planning UAS-based forest remote sensing. The effects of flight speed on modeling forest attributes like AGB need to be evaluated across a wider range of speeds and cross compared between sensor (rolling vs global shutter) and UAS platform types (multi-rotor vs fixed-wing; Zarco-Tejada et al., 2014).

Inclusion of the NGRR point cloud distribution metrics significantly improved the prediction of AGB in terms of variance explained (ΔR^2) and precision (ΔRMSE) over the Standard point cloud predictions. When NGRR metrics were included, they accounted for ~23% of important random forest predictors, with ~18% of them coming from the Stem point cloud metrics. The improved model performance, despite using only RGB spectral information, suggests that spectral segmentation of photogrammetric point clouds may be a powerful tool for improving models of forest structural attributes. Our results are shared by other studies, which found that including spectral indices from image orthomosaics as predictors of forest structure and biomass significantly improved model performance (Domingo et al., 2019). There is reason to believe more advanced segmentation and characterization of SfM points beyond indices available from RGB imagery could further improve the modeling of forest biomass done in this study. The inclusion of a greater range of spectral data from more powerful multispectral sensors may contribute to better discernment between vegetation structural components within SfM point clouds.

1.4.2 Implications for Forest Management

Increasingly UAS are being utilized for characterizing forest structure across many ecosystems and forest management objectives (Kattenborn et al., 2014; Goldbergs et al., 2018; Navarro et al., 2020). Such UAS approaches can provide data at previously unachievable temporal and spatial resolutions with relatively low operational costs compared to similar datasets from aerial LiDAR. In order to transition UAS SfM forest structure monitoring from the research realm to a management tool, standardization of flight parameter reporting is critical. Without common reporting standards, synthesis and advancements in UAS research will be limited. This study highlights the potential of UAS SfM plot-based AGB modeling and the implications of flight altitude and speed while stating the importance of reporting altitude and vegetation height for improved data interpretation.

Strong trends across all flights were found between altitude and data collection time, data processing time, and data density, all of which are important in UAS flight planning for forest mapping (Figure 1.9). Wider image footprints at higher altitudes provide more efficient flight times (~2 min ha^{-1}), while there was a fivefold increase in flight times at the lowest altitude. Similarly, there are fewer images required at higher altitudes, resulting in SfM point cloud generation times varying from 10-60 min ha^{-1} moving from the highest to lowest altitudes. Conversely, the benefits of higher flight altitude on data collection and processing time reverse, resulting in much lower point densities at the highest altitudes (~1,000 points m^{-2}) compared to lower altitudes (~7,000 points m^{-2}). While this is a strong gradient in data density, the highest altitude flights still provide greater than 50 times the point density of what is considered high quality aerial LiDAR data (Nelson, 2013). These results point to relatively rapid and reliable plot-based AGB modeling from UAS SfM at altitudes above four times a site's Lorey's Height. Additionally, moderate increases in UAS flight speed would amplify these benefits without detrimentally impacting model performance (Table 1.2).

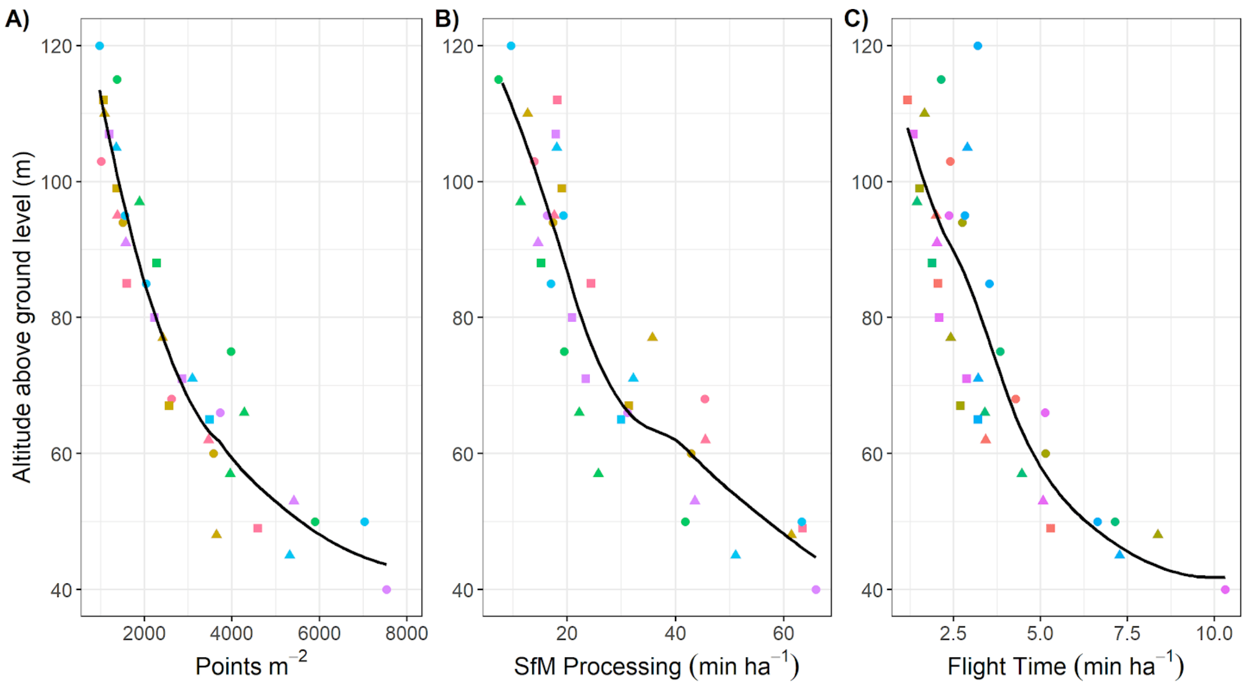

Figure 1.9. Evaluation of the effect of flight altitude above ground level on (**A**) filtered Standard SfM point cloud density, (**B**) SfM processing time in minutes ha^{-1}, and (**C**) flight time in minutes ha^{-1}, with black lines depicting Loess curves to represent data trend.

The plot-based UAS modeling strategy used in this study appears to be effective at describing forest attributes that lend themselves to imputation methods, with the aerial LiDAR literature indicated it should lend itself to describing forest biomass, basal area, and volume. While this strategy was successful at describing plot and therefore stand-level AGB, further exploration is needed to understand the potential of UAS to characterize things at both tree and landscape scales. The ultra-high resolution of UAS data products and potential to fuse spectral and structural characteristics should enable improved individual tree observations. Early testing of single tree extraction methods from UAS SfM data has successfully identified

>90% of trees (Silva et al., 2016). Characterization of individual trees with such high reliability will enable modeling of future stand conditions. Additionally, UAS have the potential to serve as a sampling tool themselves, vastly increasing the amount of data available for training courser landscape-scale satellite-based models of forest biomass. Recent research has demonstrated techniques for scaling UAS observations to describe biomass at greater extents than the UAS was capable of characterizing (Navarro et al., 2019).

1.5 Conclusion

This study demonstrates the high potential of plot-based UAS photogrammetry for modeling ponderosa pine aboveground biomass. When flying at altitudes of more than four times a forest's Lorey's Height, UAS SfM biomass modeling resulted in a 7.8% improvement in R^2 over aerial LiDAR. Additionally, segmenting the SfM point cloud based on the image spectral signature tied to individual points to look at Stem and Canopy distributions provided further substantial improvements to the AGB modeling. Beyond improved model performance, higher altitude UAS flights provide more efficient image acquisition and photogrammetry processing times of ~12 mins ha^{-1} as opposed to >70 min ha^{-1} at the lowest tested altitudes. This study highlights the role of UAS acquisition parameters on plot-based forest biomass modeling, while also showing the strong potential for UAS-based forest monitoring at increased temporal frequencies than have been feasible from aerial LiDAR. Further work is needed to understand how such acquisition parameters might influence UAS-based single tree monitoring.

Cited Works

Anderegg, W.R., Hicke, J.A., Fisher, R.A., Allen, C.D., Aukema, J., Bentz, B., Hood, S. Lichstein, J.W., Macalady, A.K., McDowell, N., Pan, Y., Raffa, K., Sala, A., Shaw, J.D., Stephenson, N.L., Tague, C., and Zeppel, M. 2015. Tree mortality from drought, insects, and their interactions in a changing climate. New Phytologist, 208(3): 674-683, doi: 10.1111/nph.13477.

Bates, D., Maechler, M., Bolker, B., and Walker, S. 2015. Fitting Linear Mixed-Effects Models Using lme4. Journal of Statistical Software, 67(1): 1-48, doi: 10.18637/jss.v067.i01.

Bouvier, M., Durriey, S., Fournier, R.A., and Renaud, J.P. 2015. Generalizing Predictive Models of Forest Inventory Attributes Using an Area-Based Approach with Airborne LiDAR Data. Remote Sensing of Environment, 156: 322–334., doi: 10.1016/j.rse.2014.10.004.

Boyden, S., Binkley, D., and Shepherd, W. 2005. Spatial and temporal patterns in structure, regeneration, and mortality of an old-growth ponderosa pine forest in the Colorado Front Range. Forest Ecology and Management, 219(1): 43-55.

Breiman, L. 2001. Random forests. Machine Learning, 45: 5-32.

Briggs, J.S., Fornwalt, P.J., and Feinstein, J.A. 2017. Short-term ecological consequences of collaborative restoration treatments in ponderosa pine forests of Colorado. Forest Ecology and Management, 395: 69-80, doi: 10.1016/j.foreco.2017.03.008.

Dandois, J.P., Olano, M., and Ellis, E.C. 2015. Optimal altitude, overlap, and weather conditions for computer vision UAV estimates of forest structure. Remote Sensing, 7(10): 13895-13920, doi: 10.3390/rs71013895.

Dixon, G.E. 2002. Essential FVS: A user's guide to the Forest Vegetation Simulator. USDA Forest Service, Internal Report, Forest Management Service Center, 204 p.

Domingo, D., Ørka, H.O., Næsset, E., Kachamba, D., and Gobakken, T. 2019. Effects of UAV Image Resolution, Camera Type, and Image Overlap on Accuracy of Biomass Predictions in a Tropical Woodland. Remote Sensing, 11(8): 948, doi: 10.3390/rs11080948.

Fraser, B.T., and Congalton, R.G. 2018. Issues in Unmanned Aerial Systems (UAS) Data Collection of Complex Forest Environments. Remote Sensing, 10: 908.

Frey, J., Kovach, K., Stemmler, S., and Koch, B. 2018. UAV Photogrammetry of Forests as a Vulnerable Process. A Sensitivity Analysis for a Structure from Motion RGB-Image Pipeline. Journal of Remote Sensing, 10(6): 912, doi: 10.3390/rs10060912.

Fritz, A., Kattenborn, T., and Koch, B. 2013. UAV-based photogrammetric point clouds-Tree stem mapping in open stands in comparison to terrestrial laser scanner point clouds. International Archive of Photogrammetry & Remote Sensing Spatial Information Science, 40: 141-146.

Goldbergs, G., et al. 2018. Efficiency of Individual Tree Detection Approaches Based on Light-Weight and Low-Cost UAS Imagery in Australian Savannas. Remote Sensing, 10(2): 161, doi: 10.3390/rs10020161.

Hernández-Santiago, J.L., Reyes-Palomeque, G., Castillo-Santiago, M.Á., George-Chacón, S.P., Huechancona-Ruiz, A.H., Tun-Dzul, F., Dondon-Rivera, D., and Dupuy, J.M. 2018. Effects of sample plot size and GPS location errors on aboveground biomass estimates from LiDAR in tropical dry forests. Remote Sensing, 10: 1586, doi: 10.3390/rs10101586.

Hummel, S., Hudak, A.T., Uebler, E.H., Falkowski, M.J., and Megown, K.A. 2011. A comparison of accuracy and cost of LiDAR versus stand exam data for landscape management on the Malheur National Forest. Journal of Forestry, 109(5): 267-273.

Hudak, A.T., Crookston, N.L., Evans, J.S., Falkowski, M.J., Smith, A.M., Gessler, P.E., and Morgan, P. 2006. Regression modeling and mapping of coniferous forest basal area and tree density from discrete-return lidar and multispectral satellite data. Canadian Journal of Remote Sensing, 32(2): 126-138, doi: 10.5589/m06-007.

Hudak, A.T., Evans, J.S., and Smith, A.M.S. 2009. LiDAR Utility for Natural Resource Managers. Remote Sensing, 1(4): 934–951, doi: 10.3390/rs1040934.

Iglhaut, J., Cabo, C., Puliti, S., Piermattei, L., O'Connor, J., and Rosette, J. 2019. Structure from motion photogrammetry in forestry: a review. Current Forestry Reports, 5: 155-168, doi: 10.1007/s40725-019-00094-3.

Jenkins, J.C., Chojnacky, D.C., Heath, L.S., and Birdsey, R.A. 2003. National-scale biomass estimators for United States tree species. Forest Science, 49(1): 12-35, doi: 10.1093/forestscience/49.1.12.

Keyser, C.E. and Dixon, G.E. 2008. Central Rockies (CR) Variant Overview – Forest Vegetation Simulator. Internal Rep. Fort Collins, CO: U. S. Department of Agriculture, Forest Service, Forest Management Service Center. 70 p.

Liaw, A. and Wiener, M. 2002. Classification and Regression by randomForest. R News 2(3), 18--22.

Lutz, J.A. 2015. The evolution of long-term data for forestry: large temperate research plots in an era of global change. Northwest Science, 89(3): 255-269.

Mitchell, A.L., Rosenqvist, A., and Mora, B. 2017. Current remote sensing approaches to monitoring forest degradation in support of countries measurement, reporting and verification (MRV) system for REDD+. Carbon Balance and Management, 12(9): 1-22.

Murphy, M.A., Evans, J.S., and Storfer, A.S. 2010. Quantify Bufo boreas connectivity in Yellowstone National Park with landscape genetics. Ecology, 91: 252-261.

Navarro, J.A., Algeet, N., Fernández-Landa, A., Esteban, J., Rodriguez-Noriega, and Guillén-Climent, M. 2019. Integration of UAV, Sentinel-1, and Sentinel-2 Data for Mangrove Plantation Aboveground Biomass Monitoring in Senegal. Remote Sensing, 11(1): 77, doi: 10.3390/rs11010077.

Navarro, J.A., Young, M., Allan, B., Carnell, P., Macreadie, P., and Ierodiaconou, D. 2020. The application of Unmanned Aerial Vehicles (UAVs) to estimate above-ground biomass of mangrove ecosystems. Remote Sensing of Environment, 242: 111747, doi: 10.1016/j.rse.2020.111747.

Nelson, R. 2014. How did we get here? An early history of forestry lidar. Canadian Journal of Remote Sensing, 39: S6-S17, doi: 10.5589/m13-011.

O'Connor J., Smith, M.J., and James, M.R. 2017. Cameras and setting for aerial surveys in the geosciences: optimising image data. Progress in Physical Geography: Earth and Environment, 41(3): 325-344, doi: 10.1177/0309133317703092.

Pan, Y., Birdsey, R.A., Phillips, O.L., and Jackson, R.B. 2013. The Structure, Distribution, and Biomass of the Worlds Forests. Annual Review of Ecology, Evolution, and Systematics, 44(1), 593-622, doi: 10.1146/annurev-ecolsys-110512-135914

R Core Team. 2019. R: A language and environment for statistical computing. R Foundation for Statistical Computing, Vienna, Austria.

Roussel, J.R. and Auty, D. 2019. lidR: Airborne LiDAR Data Manipulation and Visualization for Forestry Applications. R package version 2.0.2.

Seifert, E., Seifert, S., Vogt, H., Drew, D., Aardt, J. V., Kunneke, A., and Seifert, T. 2019. Influence of Drone Altitude, Image Overlap, and Optical Sensor Resolution on Multi-View Reconstruction of Forest Images. Remote Sensing, 11(10): 1252, doi: 10.3390/rs11101252

Silva, Carlos A., et al. 2016. Imputation of individual longleaf pine (Pinus palustris Mill.) tree attributes from field and LiDAR data. Canadian Journal of Remote Sensing, 42(5): 554-573, doi: 10.1080/07038992.2016.1196852.

Thiel, C. and Schmullius, C. 2016. Comparison of UAV Photograph-Based and Airborne Lidar-Based Point Clouds over Forest from a Forestry Application Perspective. International Journal of Remote Sensing, 38(8-10): 2411-2426, doi:10.1080/01431161.2016.1225181.

Tinkham, W.T., Smith, A.M.S., Affleck, D.L.R., Saralecos, J.D., Falkowski, M.J., Hoffman, C.M., Hudak, A.T., and Wulder, M.A. 2016. Development of height-volume relationships in second growth Abies grandis for use with aerial LiDAR. Canadian Journal of Remote Sensing, 42(5): 400-410, doi: 10.1080/07038992.2016.1232587.

Torresan, C., Berton, A., Carotenuto, F., Gennaro, S.F.D., Gioli, B., Matese, A., … Wallace, L. 2016. Forestry applications of UAVs in Europe: a review. International Journal of Remote Sensing, 38(8-10), 2427-2447, doi: 10.1080/01431161.2016.1252477

Torres-Sánchez, J., López-Granados, F., Serrano, N., Arquero, O., and Peña, J.M. 2015. High-Throughput 3-D Monitoring of Agricultural-Tree Plantations with Unmanned Aerial Vehicle (UAV) Technology. PLoS ONE, 10(6): e0130479.

Vogeler, J.C., Yang, Z., and Cohen, W.B. 2016. Mapping post-fire habitat characteristics through the fusion of remote sensing tools. Remote Sensing of Environment, 173: 294-303, doi: 10.1016/j.rse.2015.08.011

Wallace, L., Lucieer, A., Malenovský, Z., Turner, D., and Vopěnka, P. 2016. Assessment of Forest Structure Using Two UAV Techniques: A Comparison of Airborne Laser Scanning and Structure from Motion (SfM) Point Clouds. Forests, 7: 62.

Webster, C., Westoby, M., Rutter, N., and Jonas, T. 2018. Three-dimensional thermal characterization of forest canopies using UAV photogrammetry. Remote Sensing of Environment, 209: 835-847, doi: 10.1016/j.rse.2017.09.033

Zarco-Tejada, P., Diaz-Varela, R., Angileri, V., and Loudjani, P. 2014. Tree height quantification using very high resolution imagery acquired from an unmanned aerial vehicle (UAV) and automatic 3D photo-reconstruction methods. European Journal of Agronomy, 55: 89-99.

Chapter 2: INVESTIGATING THE INFLUENCE OF CROSSHATCH AND OFF-NADIR UAS IMAGERY FOR SINGLE TREE DETECTION

2.1 Introduction

The increasing focus on restoration of forest structural variation and spatial pattern (Tinkham et al., 2017; Addington et al., 2018) in dry conifer forests has led to a greater emphasis on forest monitoring strategies that can be summarized across scales (Cannon et al., 2018). At fine spatial scales, restoration objectives in these forested systems emphasize creating a variable matrix of groups and openings, while also reducing the prevalence of small trees that have established in the absence of an intact frequent fire regime (Allen et al., 2002). Promoting variable density tree groups with openings between groups can increase forest resilience to fire (Ziegler et al., 2017). Fine scale restoration objectives also include retention of dense groups and patches of older trees for tree squirrels, snags for woodpeckers and secondary-cavity nesting species, and logs for invertebrate species and small mammals (Reynolds et al., 2013). At broader spatial scales, restoring heterogeneity within stands and in-between stands is critical for moving dry conifer forest systems towards historical conditions that balanced resilience to disturbance with providing a diversity of habitat structures (North et al., 2009). To inform these restoration objectives with data sources that can be summarized across scales from groups of trees to entire stands, different strategies such as light detection and ranging (LiDAR) have been explored.

In the past 30 years, research focused on forest structure modeling has investigated using both aerial LiDAR (ALS) and terrestrial LiDAR (TLS) to acquire three-dimensional point returns to estimate first-order properties like a tree's location, height, and stem diameter (Hopkinson et al., 2004; You et al., 2016), as well as derive second-order properties like basal area and timber volume per hectare (Nilsson, 1996; Tinkham et al., 2016). ALS datasets commonly range from 0.5-60 points m^{-2} and have been widely tested across a range of types, densities, and complexities for assessing individual tree characteristics (Wilkes et al., 2015; Kandare et al., 2016). Single tree detection accuracies from ALS point cloud-derived canopy height models (CHM) range from 40-94%, with detection rates decreasing as forest complexity and density increase (Falkowski et al., 2006; Silva et al., 2016; Sačkov et al., 2019). Most omitted trees from these techniques tend to occupy lower portions of the forest canopy. The use of TLS is newer in the field of forestry but can provide ultra-high density (25-100 thousand points m^{-2}; Saarinen et al., 2017) point clouds for sampling individual trees or plots. Despite limited spatial extent, TLS observations are now an established forest sampling tool with many studies highlighting the technological potential for characterizing individual tree stem characteristics. TLS has been found to detect 22-100% of trees, with accuracies varying across forest density (Maas et al., 2008; Heinzel and Huber, 2016); various stem extraction methods have been shown to achieve diameter at breast height (DBH; 1.37 m) precisions of 1.5-3.5 cm RMSE. When applied together, the fusion of ALS spatial extent and TLS resolution has been able to generate comprehensive structural data of forest stands (Paris et al., 2017). Unfortunately, the high equipment and operational costs of ALS, along with limited TLS spatial extent have restricted their widespread adoption in forest monitoring (Cook, 2017).This highlights a need for more cost and time efficient methods of acquiring tree level overstory and understory forest structural characteristics to inform management strategies.

Similar estimations of tree locations, height, and DBH have been attempted through structure from motion (SfM) photogrammetry, which uses a camera's properties and different image viewpoints to solve for the three-dimensional location of co-occurring pixels (Forsman et al., 2016). Testing of terrestrial SfM for stem detection has found similar detection rates to TLS, with small stand (<100 trees) demonstrations extracting 60%-98% of tree locations (Liang et al., 2014; Mokroš et al., 2018). Additionally, terrestrial SfM DBH measurement precision only decreases slightly over TLS to 5.1-7.2 cm RMSE (Forsman et al., 2016; Piermattei et al., 2019). The low cost of Unmanned Aerial Systems (UAS) has made applying SfM to imagery collected above the forest canopy a viable alternative to ALS (Dandois and Ellis, 2013; Thiel and Schmulluis, 2016).

Improving sensor technology has enabled UAS-SfM point clouds with data densities in excess of 1,000 points m^{-2} (Swayze et al., *in prep*). These high data densities enable generation of finer resolution CHMs compared to ALS, improving detection rates of suppressed and intermediate trees (Creasy et al., *in review*). In some instances, secondary forest parameters like basal area have been modeled from extracted tree densities based on local relations between density and basal area (Belmonte et al., 2020). The relatively high precision of these efforts suggests these strategies could be applied to monitor ponderosa pine forest restoration objectives. The rapidly expanding use of SfM-based photogrammetry in forestry is a ripe area for evaluating how UAS image acquisition strategies impact derived estimates of forest structure. Early exploration of flight parameters has focused on how photo overlap, flight height, and ground sampling distance impact image alignment and point cloud reconstruction quality (Dandois et al., 2015; Nesbit and Hugenholtz, 2019). While research has started to evaluate how flight parameters impact structural measurements like tree height and crown diameter (Frey et al., 2018), knowledge gaps remain regarding other structural attributes. Particularly, the impacts of UAS flight altitude and pattern along with camera angle (Figure 2.1) have received little attention for their implications on individual tree parameter assessment.

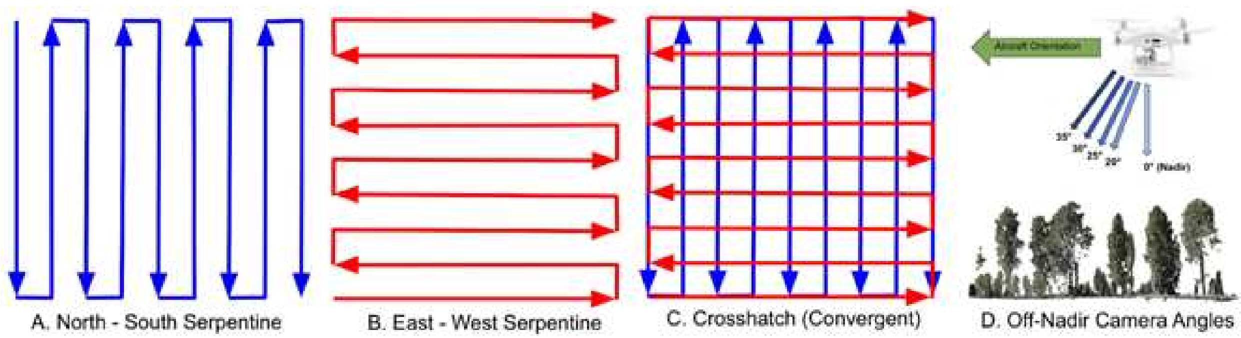

Figure 2.1. Flight pattern for N-S serpentine (A), E-W serpentine (B), crosshatch (C) and camera orientation along a flight line depicting multiple camera angle scenarios (D).

Most UAS forest photogrammetry studies utilize conventional serpentine flight patterns (Figure 2.1A) and nadir (90° to the ground; Figure 2.1D) camera view angles for generating point clouds. Nesbit and Hugenholtz (2019) found that creating a crosshatch flight (Figure 2.1C) by adding a second serpentine flight pattern (Figure 2.1B) of off-nadir (20-35°) UAS images to a nadir serpentine dataset improved digital terrain model precision. Additionally, adding 15° oblique imagery to nadir imagery datasets in deciduous and coniferous forest leaf-on and leaf-off conditions increased understory point cloud density (Díaz et al., 2020). The use of off-nadir 45° camera angles provided reliable stem reconstruction of ~70% of trees in a leaf-off deciduous forest (Fritz et al., 2013); however, the authors speculated that altering the camera orientation during crosshatch flight paths to provide a diversity of camera orientations could further improve stem identification and DBH extraction. Hybrid SfM photogrammetry approaches that utilize both UAS and terrestrially collected images can provide RMSE of less than 1 cm and 1 m for tree DBH and height, respectively (Mikita et al., 2016). While being highly precise, the smaller extent of terrestrial image collection limits such direct tree observations through data fusion.

Since preliminary testing of crosshatch and off-nadir UAS data acquisition methods indicate improved point density in the lower canopy and stem region (Díaz et al., 2020), it is logical to more thoroughly investigate the impact of these variables on extracted tree parameters like DBH. However, as it is unlikely UAS point clouds generated from images acquired above the forest canopy will directly characterize DBH of all trees, other techniques of filling missing DBH values are needed in order to directly summarize basal area or apply common allometries of tree volume and biomass. Imputation of missing values in forest growth and yield modeling systems commonly occurs by using paired DBH and height values from forest inventories to calibrate regional relationships of DBH predicting height in order to fill in missing heights within the inventory (Dixon, 2002). This same strategy has potential to be reversed to predict missing DBH values from correctly extracted DBH and height observations from UAS point clouds.

This study investigates the influence of UAS flight parameters on modeling individual tree and stand-level metrics from UAS developed height to DBH relationships through a series of tasks. First, we evaluate the impact of UAS flight altitude, camera angle, and flight path on UAS CHM individual tree detection rates and UAS-SfM point cloud extracted tree height and DBH accuracy. Next, a regional height to DBH relationship is applied to filter UAS extracted tree height and DBH observations, which are then used to develop a local height to DBH model to predict missing UAS DBH values. Finally, we evaluate the effect of flight parameters on the precision of plot and stand level estimates of overstory (> 6 m tall) basal area (m^2 ha^{-1}) and trees per hectare, along with understory trees per hectare.

2.2 Methods

The study workflow (Figure 2.2) consisted of four components: 1) data collection, 2) tree extraction, 3) data filtering and modeling, and 4) data analysis and validation. First, UAS imagery and stem map data was collected in the field. Second, UAS imagery was processed to generate point clouds and CHMs. Third, tree heights and DBHs were extracted from UAS datasets. These extracted heights and DBHs were spatially paired, filtering against a regional height to DBH relationship, and used to model missing DBH values. Fourth, commission and omission errors were calculated for extracted trees, and the accuracy and precision of tree height, DBH, and overstory and understory stand density.

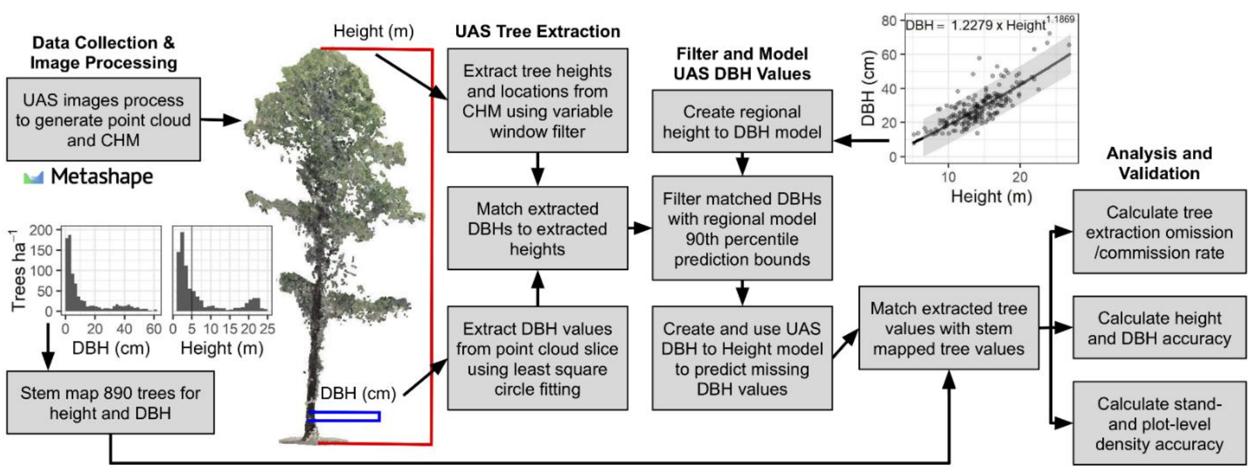

Figure 2.2. Integrative workflow of the data collection and processing, tree matching, and analysis steps used to assess accuracy of UAS extracted tree- and stand-level characteristics.

2.2.1 Study Area and Field Data

This study was conducted in the Manitou Experimental Forest, about 40 km northwest of Colorado Springs, Colorado. A 1 hectare (100 x 100 m) stem map of ponderosa pine (*Pinus* *ponderosa* var. *scopulorum* Dougl. Ex Laws.) dominated forest was established for validation. All trees > 1.37 m tall (n=890) were mapped and inventoried using a grid of survey points distributed across the site with observations of tree height and DBH recorded in August 2018. The site exhibits a multi-age forest structure, due to regeneration pulses following a shelterwood style harvest in the 1880's and pine beetle disturbance in the 1980's (Boyden et al., 2005). The inventory demonstrates a stand structure with increased density beyond historical levels within the region (Battaglia et al., 2018), with enough overstory shading to allow five Douglas-fir (*Pseudotsuga menziesii* (Mirb.) Franco var. *glauca* (Beissn.) Franco) and two blue spruce (*Picea pungens* Engelm.) to establish in the understory. Dividing the stand into two strata at a 5 m tall breakpoint shows 374 trees ha^{-1} and 24.32 m^2 ha^{-1} of basal area in the overstory tree stratum and 506 trees ha^{-1} in the understory tree stratum (see inset of tree size distributions in Figure 2.2). We selected the 5m threshold as it roughly corresponds to a 10 cm DBH, a common regional forest inventory breakpoint for describing overstory and understory forest densities, where the understory includes what is commonly referred to as sapling or advanced regeneration.

2.2.2 Regional Field Data

For development of a regional height to DBH relationship, we acquired USA Forest Service Forest Inventory and Analysis (FIA) data (Tinkham et al., 2018) for 6,693 plots in the state of Colorado. We filtered plots to only retain those containing >70% ponderosa pine basal area and with a site index within ±2 m of the study area's site index, leaving 92 plots with 196 trees. We fit a power function to predict DBH as a function of height using the nlme package (Pinheiro et al., 2018) in the R statistical program. We generated 90th percentile prediction bounds for the model (see inset model graph in Figure 2.2) to filter UAS extracted DBH values that were matched with UAS extracted heights.

2.2.3 UAS Image Collection

We conducted a total of 30 UAS flights over the 1 hectare study area in July 2019, collecting approximately 7,140 images in 4.66 hours of in-air flight time. The imagery was collected with a Da-Jiang Innovations (DJI) Phantom 4 Pro UAS, with a 1 inch 20 MP (5472 x 3648 pixels) metal oxide semiconductor red-green-blue (RGB) sensor at a fixed 8.8 mm focal length. Flights were conducted at three altitudes above ground level (65, 90, and 115 m) with 90% front and side image overlap at 4 m sec^{-1}, over a 110 x 110 m size grid centered on the 1 hectare study area. Altizure (version 4.6.8.193; Shenzhen, China) for Apple iOS was used to acquire nadir imagery using separate North-South (NS) and East-West (EW) camera orientations at each altitude for a total of six nadir image acquisitions. Then Pix4D Capture (Pix4D S.A., Laussanne, Switzerland) was used to acquire off-nadir imagery (20, 25, 30, and 35°) using separate NS and EW camera orientations at each altitude, a total of 24 off-nadir acquisitions.

2.2.4 UAS Image SfM Processing and Filtering

We utilized Agisoft Metashape to process the imagery from the 30 flights. This was done by first finding matching tie points and aligning the photos, generating the sparse point cloud, georeferencing the imagery, and then finally creating dense RGB point clouds. These consisted of 15 serpentine NS and 15 crosshatch SfM point clouds distributed across three altitudes and five camera angles. The Metashape SfM processing followed the workflow presented in Swayze et al. (*in prep*), including ten ground control points collected using a Trimble GeoXT (Trimble Inc., Sunnyvale, CA, USA) with SBAS real-time correction accuracies of < 1 m.

After the SfM processing, dense point clouds were filtered to remove erroneous points below ground and above the canopy and classified into ground and non-ground using LAStools version 1.2 (http://lastools.org). Following point filtering and classification, the point clouds were normalized using the classified ground points, and the normalized point clouds were rasterized into 10 cm resolution CHMs. To prepare the SfM point cloud data for DBH extraction, the 30 normalized point clouds were merged into a single “hyper-cloud” file. From the hypercloud (900+ million point) vertical sections of the stem (0.5-5 m) and canopy (24-27 m) were extracted. Next, 60 random sample locations from the hypercloud stem and canopy segments were manually extracted in CloudCompare version 2.10.1 (www.cloudcompare.org) to obtain pure stem and canopy points. The extracted sample points (>800,000 points in each class) were imported into the R statistical programming language (R core Team, 2019) using the lidR package (Roussel and Auty, 2019), where a green:red ratio index (NGRR; Equation 1) was calculated on each point to determine the distribution (Figure 2.3A) of stem and canopy NGRR values. All values below the 90th percentile of stem NGRR values (-0.0152) were segmented from each SfM point cloud to produce point clouds only containing points with stem reflectance characteristics. From the stem point clouds, a 10 cm tall slice (1.32-1.42 m) was extracted and compressed to a height of 1.37 m to represent the DBH region on the trees. An example of this process on a single point cloud stem is displayed in Figure 2.3C. These DBH slices were later used to extract individual tree DBH values.

$$NGRR = \frac{G_{band} - R_{band}}{G_{band} + R_{band}} \qquad \text{[Equation 1]}$$

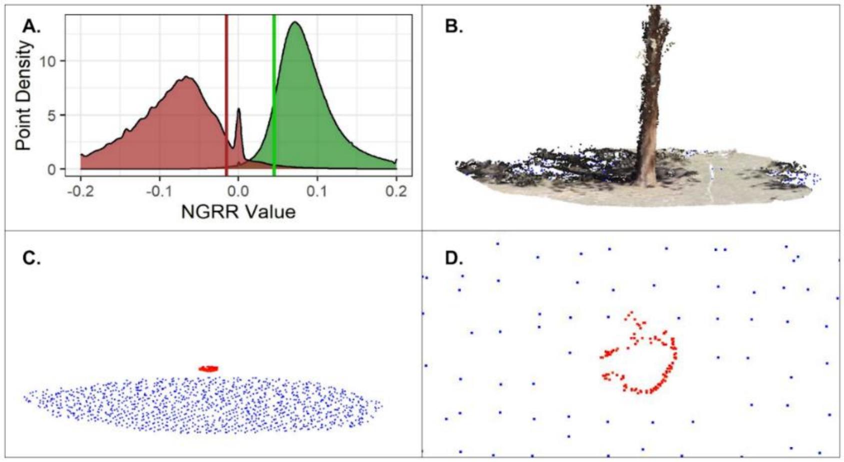

Figure 2.3. Distribution of NGRR values for stem (brown) and canopy (green) points, with vertical lines representing the 90th percentile of stem (brown; -0.0152) and 10th percentile of canopy (green; 0.0451) (A) example stem point cloud following NGRR segmentation (B), 10 cm DBH slice (1.32-1.42 m) with thinned ground points (C), and top-down view of stem segment (D) with stem points shown in red.

2.2.5 Tree Location and Height Extraction

All 30 SfM-derived 10 cm resolution CHMs were analyzed to detect individual tree locations and heights using a local maximum variable window function (Popescu and Wynne, 2004) from the R ForestTools package (Plowright, 2018). The local maximum function searches each CHM to identify local maximum heights within a variable radius moving window based on the rasterized tree heights, assigning a point to locations with defined maximums. The function was parameterized using a linear equation (Equation 2) to determine the window radius based on research by Creasy et al. (*in review*), who found similar parameters for optimizing tree detection across all tree sizes in similar forest systems.

$$variable\ window\ radius = Tree\ Height \times 0.1 \qquad \text{[Equation 2]}$$

Where the *variable window radius* is in meters and *Tree Height* is in meters and corresponds to raster cell values in the CHM. The algorithm was parameterized to extract locations and maximum heights of trees > 1.37 m tall in the 30 CHMs. The outputs from the tree location and height extraction step included x and y locations paired with a height estimate in meters, here on referred to as extracted tree heights.

2.2.6 Tree DBH Extraction

The DBH point cloud slices were analyzed using the R TreeLS package (Conto, 2019), following a workflow presented in Conto et al. (2017). The point cloud slices were rasterized so a Hough Transform circle search algorithm could be used to identify candidate DBH locations with a minimum density setting of 0.001. At each candidate DBH location, a least squares circle fitting algorithm was used on the DBH point cloud slice to estimate DBH. This step utilized a random sample consensus approach to identify points to keep by iteratively fitting least squares circles to candidate DBH locations until the sum of squared distances between the circle and points was minimized, with a tolerance of 0.025 and confidence level of 0.99. For candidate DBH locations that successfully fit a circle, the process generated estimated x and y coordinates and DBH values, here on referred to as extracted tree DBHs.

2.2.7 Matching Extracted Values with Field Observations

For each UAS acquisition the extracted tree DBHs were matched with extracted tree heights through a multi-stage filtering process. We first predicted DBH values for each extracted tree height using the regional FIA height to DBH relationship. We then compared FIA predicted DBH values with extracted tree DBHs, identifying matches by iteratively buffering a FIA predicted DBH value using a 4 m radius to account for tree lean and to identify candidate extracted tree DBHs. The candidate extracted tree DBH with the smallest difference to the FIA predicted DBH was assigned to the extracted tree height. Once all extracted tree DBHs had been assigned to an extracted tree height, the paired extracted tree heights and DBHs were filtered to only keep extracted tree DBHs conforming to the 90th percentile prediction bounds of the regional FIA height to DBH relationship. The outputs from the matching and 90th percentile filtering process are here after referred to as paired extracted tree values.

The 30 paired extracted tree value datasets were then each matched with the field observed tree values. After selecting candidate stem map trees within 4 m of a paired extracted tree value, the difference between field observed and extracted tree heights was calculated. A successful match required < 2 m height error; after a successful match the paired fielded observed and extracted heights are removed from the pool of candidates for further matching. This matching was repeated until all paired extracted tree values were either matched to a stem map tree or were marked as omissions (having no match within 4 m and < 2 m height difference). True Positive, False Negative, and False Positive rates were calculated for paired extracted tree values and stem mapped trees. The quality of each dataset was summarized by calculating recall, precision, and F-score using equation 3, 4, and 5, respectively.

$$Recall = \frac{True\ Positive}{True\ Positive + False\ Negative} \quad \text{[Equation 3]}$$

$$Precision = \frac{True\ Positive}{True\ Positive + False\ Positive} \quad \text{[Equation 4]}$$

$$F - score = 2 \times \frac{Recall \times Precision}{Recall + Precision} \quad \text{[Equation 5]}$$

2.2.8 DBH Prediction and Stand Parameter Estimation

For each dataset, we used the paired extracted tree value estimates of DBH and height to develop a local predictive model of DBH as a function of height using a power equation. We applied these predictive models to the extracted tree heights not matched with an extracted DBH value and merged these with the paired extracted tree values to generate a complete dataset of UAS estimated heights and DBHs for each of the 30 datasets. Mean error (ME) and root mean square error (RMSE) of the final extracted height and DBH values were determined for the 30 SfM extracted datasets to describe the bias and precision of extracted values.

To assess the accuracy of stand-level density metrics, the field observed trees were divided into a 20 x 20 m grid of plots and summarized as trees ha^{-1} (TPH) for trees > 6 m tall and ≤ 6 m tall for each plot and across the entire study area. Additionally, basal area (m^2 ha^{-1}) was similarly summarized for trees > 6 m tall. For each UAS dataset, we also summarized identical TPH and basal area metrics from the paired extracted tree values. We determined correlation and RMSE by comparing the observed and extracted TPH and basal area at the 20 x 20 m plot level, while the absolute error was summarized at the stand level (1 hectare) for each metric.

2.2.9 Assessment of Altitude, Pattern, and Camera Angle

We used multiple linear regression to determine the influence of tested UAS flight parameters (camera angle, flight altitude, and flight path) on tree extraction performance metrics (F-score, precision, and recall). Additional models were generated to describe how flight parameters impacted the correlation, ME, and RMSE of extracted tree heights and DBH values. The main effects of altitude, camera angle, and flight path were evaluated for interactions in all regression models through a forward and backward AIC stepwise selection algorithm to determine the best variable subset that minimized the AIC value. Modeling was performed using the lm and stepAIC functions of the stats (R Core Team, 2019) and MASS R packages (Venables and Ripley, 2002). All main effects were kept in the final model regardless of if they were statistically significant or not.

2.3 Results

2.3.1 Extracted Tree Detection Performance

Extraction quality metrics (F-score, precision, and recall) for trees > 1.37 m tall varied in their relationship with UAS camera angle and flight pattern according to multiple linear regression (Table 2.1). Overall performance of correct tree detection and matching as described by F-score was significantly increased by ~4% for crosshatch flight patterns compared to serpentine. F-score values for extracted tree locations varied from 0.429 to 0.771 with a decreasing trend as camera angle increased, with average scores varying from 0.739 to 0.626 for nadir and 35° off-nadir flights, respectively (Figure 2.4). Across testing, crosshatch flight patterns paired with nadir camera angles provided the highest SfM tree extraction F-scores.

Table 2.1. Multiple linear regression results on the effect of UAS acquisition parameters on the reliability of extracted trees. Serpentine flight pattern was treated as the base predictor (coefficient = 0). Significant parameters (α = 0.05) indicated in boldface.

Parameter	Coefficient	Standard Error	t-value	p-value	Adj. R^2
Response = F-score					0.1660
Intercept	0.7942	0.0639	12.426	<0.001	
Altitude (m)	-0.0004	0.0006	-0.684	0.5002	
Angle (degrees)	-0.0023	0.0011	1.815	0.0811	
Pattern (Crosshatch)	0.0337	0.0185	-2.080	**0.0475**	
Response = Precision					0.1466
Intercept	1.0470	0.1312	7.978	<0.001	
Altitude (m)	-0.0007	0.0013	-0.536	0.5967	
Angle (degrees)	-0.0053	0.0022	-2.373	**0.0253**	
Pattern (Crosshatch)	0.0108	0.0381	0.283	0.7796	
Response = Recall					0.0655
Intercept	0.5867	0.0449	13.064	<0.001	
Altitude (m)	0.0001	0.0005	0.286	0.7777	
Angle (degrees)	0.0006	0.0008	0.772	0.4470	
Pattern (Crosshatch)	0.0221	0.0130	1.700	0.1010	

The proportion of extracted trees that matched field observed trees, summarized as precision, significantly decreased as camera angle increased (Table 2.1). Average extracted tree location precision varied from 0.942 to 0.669 at nadir and 35° off-nadir (Figure 2.4). Capturing the correct number of trees as described by recall only showed weak variation with flight pattern (p = 0.1010). Recall for crosshatch flight patterns averaged 0.627 while serpentine patterns averaged 0.59, suggesting crosshatch patterns were slightly closer to the correct number of trees compared to serpentine flights (Figure 2.4).

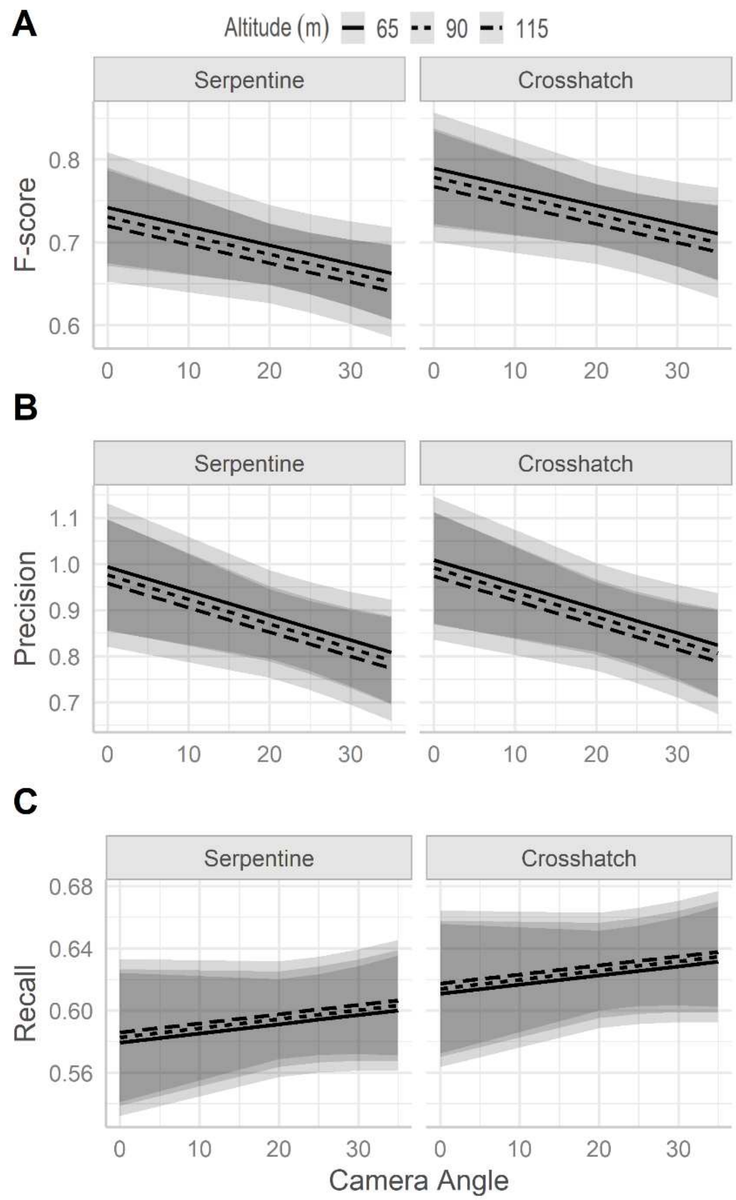

Figure 2.4. Visualization of multiple linear regression response variables (A) F-score, (B) precision, and (C) recall against predictors of altitude, camera angle, and flight pattern.

2.3.2 Extracted Tree Height and DBH Assessment

Correlation between paired extracted tree heights and field observed tree heights exceeded 0.98 for all datasets (Figure 2.5). Camera angle and flight pattern both significantly impacted height errors, with nadir camera angles underpredicting by 0.14 m on average, while 20-35° camera angles overpredicted heights by 0.17-0.12 m (Table 2.2). Crosshatch flight patterns also resulted in increased mean height errors by 0.06 m compared to serpentine patterns. The precision of extracted heights averaged a RMSE of 17.9% for nadir camera angles and significantly increased as camera angle increased from 20-35° (Table 2.2).

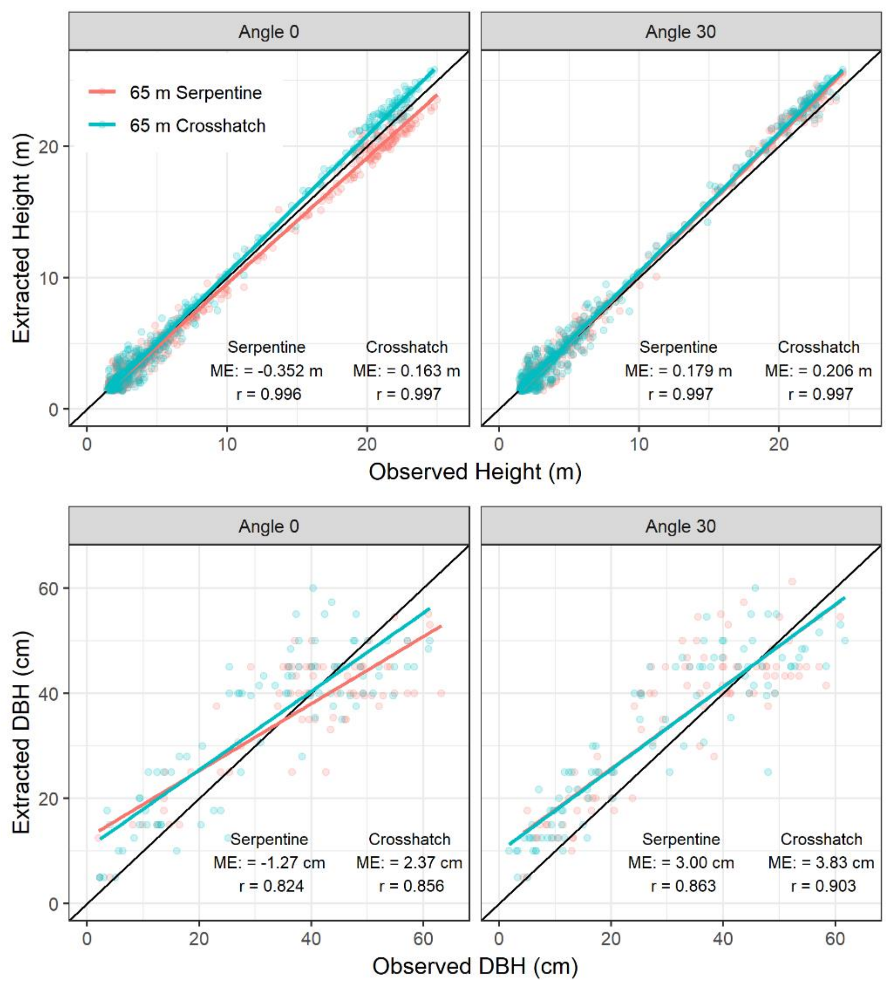

Figure 2.5. Observed versus extracted height and DBH values for the best serpentine and crosshatch acquisitions (both 65 m altitude).

Table 2.2. Multiple linear regression results of the effect of UAS acquisition parameters on bias (ME) and precision (RMSE) of extracted tree heights and DBH values meeting FIA 90th percentile prediction bounds filtering. Serpentine flight pattern was treated as the base predictor (coefficient = 0). Significant parameters (α = 0.05) indicated in boldface.

Parameter	Coefficient	Standard Error	t-value	p-value	Adj. R^2
Response = Height ME (m)					0.4648
Intercept	0.038	0.103	0.364	0.7189	
Altitude (m)	-0.001	0.001	-1.346	0.1900	
Angle (degrees)	0.008	0.002	4.668	**<0.001**	
Pattern (Crosshatch)	0.064	0.030	2.140	**0.0419**	
Response = Height RMSE (%)					0.1256
Intercept	15.466	1.215	12.731	<0.001	
Altitude (m)	0.016	0.012	1.272	0.2148	
Angle (degrees)	0.048	0.021	2.315	**0.0287**	
Pattern (Crosshatch)	-0.153	0.353	-0.434	0.6679	
Response = DBH ME (cm)					0.3555
Intercept	1.035	0.970	1.067	0.2958	
Altitude (m)	0.001	0.010	0.081	0.9364	
Angle (degrees)	0.064	0.016	3.903	**<0.001**	
Pattern (Crosshatch)	0.545	0.281	1.938	0.0635	
Response = DBH RMSE (%)					0.0548
Intercept	53.487	26.750	2.000	0.0561	
Altitude (m)	-0.138	0.269	-0.512	0.6127	
Angle (degrees)	0.895	.454	1.970	0.0595	
Pattern (Crosshatch)	-5.689	7.762	-0.733	0.4702	

Across the 30 datasets, the number of extracted tree DBHs equaled 14.2-47.8% (avg: 31.1%) of the field observed trees. After filtering the extracted tree DBHs with the FIA regional 90th percentile prediction bounds, 4.2-11.5% (avg: 8.0%) were retained as conforming to the expected height to DBH relationship. This translates to 37-103 trees kept for modeling the local height to DBH relationships. Of the tested altitudes, the 65 m flights had a greater proportion of extracted and retained (39.6 and 10.1%, respectively) DBH values following FIA regional filtering compared to higher altitude flights (25.8 and 7.2%, 28.0 and 7.1% for 90 and 115 m, respectively). Similarly, crosshatch flights had greater rates of extraction and filter retained DBH values (avg: 31.9 and 8.4%) compared to serpentine flights (avg: 27.3 and 6.5%).

For all flights the correlation between extracted tree DBHs and field observed values ranged from 0.554 to 0.886. Filtering extracted tree DBHs through the regional FIA relationship improved correlation with field observed DBHs so that they were > 0.871 for all UAS datasets. The filtered extracted tree DBH correlations were significantly higher for crosshatch flight patterns compared to serpentine flights (Figure 2.6), along with significantly increasing correlation as camera angle increased.

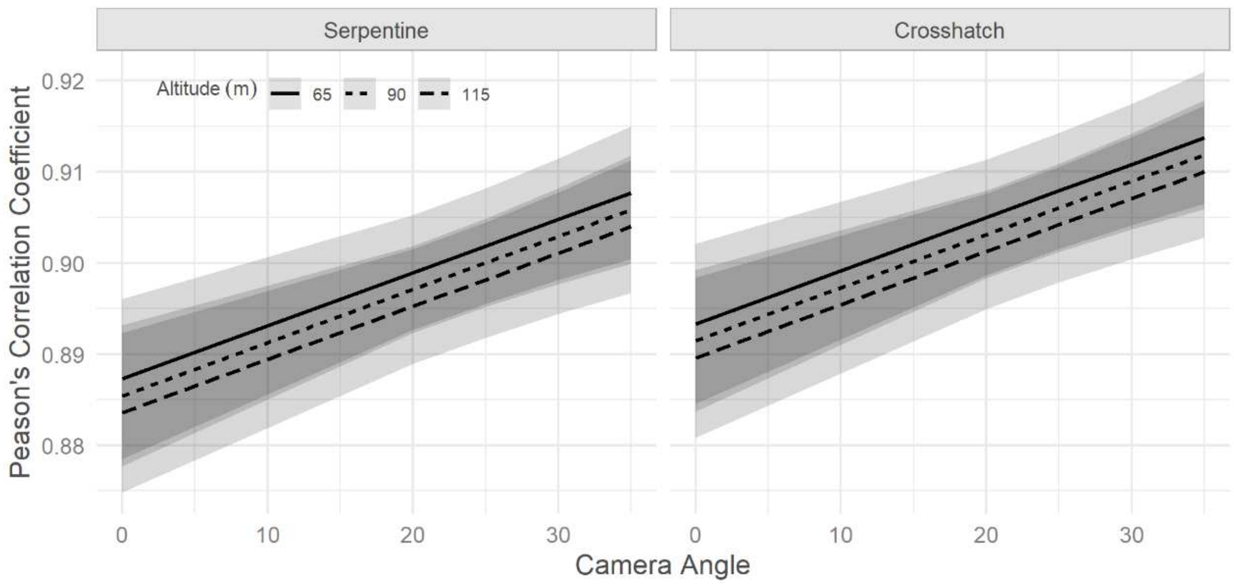

Figure 2.6. Visualization of multiple linear regression of correlation between extracted and observed DBH values against predictors of altitude, camera angle, and flight pattern.

For the filtered extracted tree DBHs there was constant overestimation bias that varied with camera angle and flight pattern (Table 2.2). Nadir acquisition DBH values had a mean error (bias) of 0.79 cm, with this increasing 0.64 cm for every 10° increase in camera angle. Similarly, DBH bias was on average 0.55 cm greater for crosshatch flight patterns compared to serpentine flights. Additionally, the RMSE of extracted and matched DBH values was 41.3% for nadir flight patterns and increased for off-nadir datasets by 8.95% for every 10° increase in camera angle.

2.3.3 Distribution of UAS Heights and DBHs

Across the datasets, the distributions of paired extracted tree heights closely followed the distribution of field observed heights (Figure 2.7). The small underprediction bias present in the nadir serpentine flights (Table 2.2) carries through during comparison of distributions (Figure 2.7). However, crosshatch flight patterns and off-nadir camera angles provided closer visual approximations of the field observed tree height distribution. The distributions of predicted tree DBHs from the UAS relationship between extracted heights and DBHs shows an underrepresentation of smaller diameter trees for serpentine acquisitions (Figure 2.7). Visual fit of the distribution for both flight patterns improved for off-nadir camera angles.

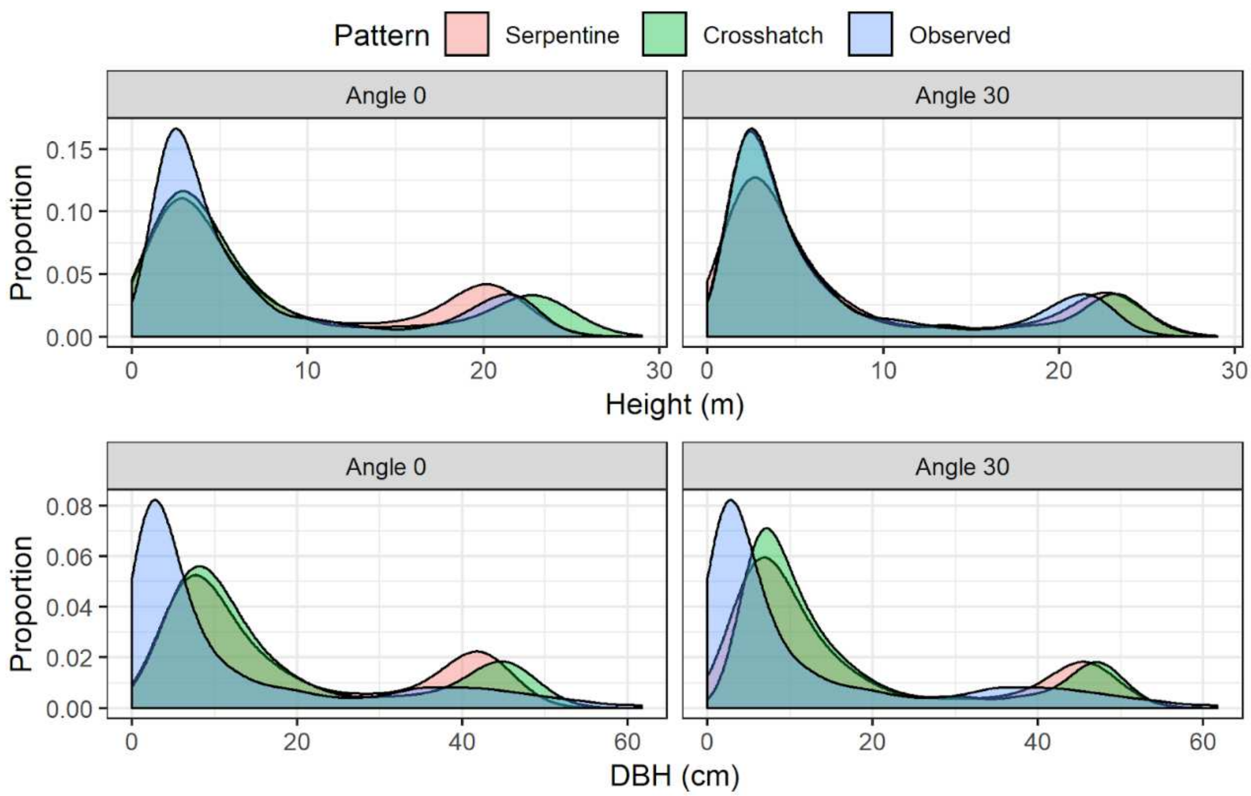

Figure 2.7. Distributional comparison of (top) extracted tree heights and (bottom) modeled UAS DBH values from 65 m altitude acquisitions against field observed heights and DBHs.

2.3.4 UAS Basal Area and TPH Accuracy

Overall, UAS 20 x 20 m plot-level estimates of overstory basal area per hectare, overstory TPH, and understory TPH had high (> 0.7) correlation with field observed values, with the exception of acquisitions using 35° off-nadir camera angles where correlations averaged less than 0.5. For overstory basal area per hectare the best acquisitions exceeded correlations of 0.8 and were at lower flight altitudes (65-90 m) with off-nadir camera angles. More than 40% of acquisitions had overstory TPH correlations exceeding 0.8, with the top eight acquisitions also exceeding 0.9 correlations for understory TPH. All the best performing acquisitions for TPH used either crosshatch or off-nadir flight designs.

Table 2.3. Multiple linear regression results on the effect of UAS acquisition parameters on summarized extracted tree density metrics. Serpentine flight pattern was treated as the base predictor (coefficient = 0). Significant parameters (α = 0.05) indicated in bold.

Parameter	Coefficient	Standard Error	t-value	p-value	Adj. R^2
Response = Understory TPH RMSE (%)					0.0745
Intercept	-96.98	145.82	-0.665	0.5119	
Altitude (m)	1.11	1.47	0.759	0.4547	
Angle (degrees)	4.78	2.48	1.929	0.0647	
Pattern (Crosshatch)	-43.09	42.31	-1.018	0.3179	
Response = Overstory TPH RMSE (%)					0.1609
Intercept	26.09	6.79	3.843	0.0007	
Altitude (m)	0.05	0.07	0.682	0.5013	
Angle (degrees)	0.32	0.12	2.814	**0.0092**	
Pattern (Crosshatch)	-0.82	1.97	-0.419	0.6788	
Response = Overstory Basal Area Hectare RMSE (%)					0.2608
Intercept	17.69	12.11	1.460	0.1563	
Altitude (m)	0.17	0.12	1.423	0.1666	
Angle (degrees)	0.64	0.21	3.134	**0.0042**	
Pattern (Crosshatch)	-4.14	3.52	-1.178	0.2496	

Camera angle significantly impacted the precision (RMSE) of plot-level estimated overstory (> 6 m tall) basal area per hectare and overstory trees per hectare (Figure 2.8). Each 10° increase in camera angle resulted in a 3.2 and 6.4% RMSE increase of plot-level overstory

TPH and BA, respectively (Table 2.3). Assessment of basal area for the entire 1 ha study site provided overestimation errors of 1-6 m^2 ha^{-1} (or 4.1-24.7%). Study site basal area errors were on average smaller for crosshatch compared to serpentine flight patterns and tended to increase with increased camera angles.

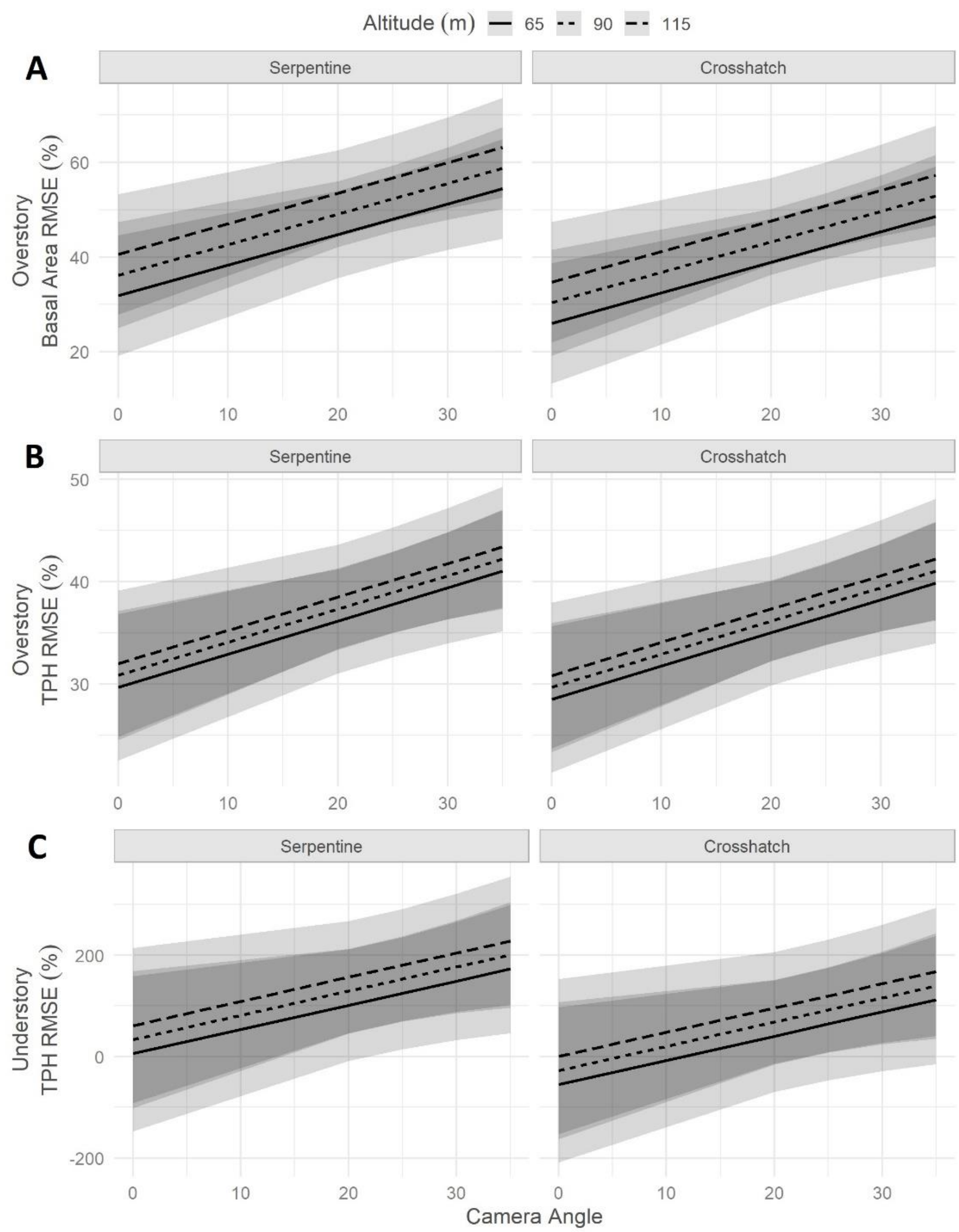

Figure 2.8. Visualization of multiple linear regression of the response variable (A) overstory basal area RMSE (%), (B) overstory TPH RMSE (%), and (C) understory TPH RMSE (%) against predictors of altitude, camera angle, and flight pattern.

2.4 Discussion

This study evaluated the impact of UAS flight altitude, camera angle, and flight path on: 1) UAS SfM individual tree detection rates; 2) extracted tree height and DBH errors; 3) local UAS-based models to predict individual tree DBH; and 4) estimates of UAS-based plot- and stand-level overstory and understory density metrics. We found that, 1) tree extraction accuracy and correctness was maximized for nadir crosshatch UAS flight designs; 2) extracted tree height precision and accuracy was high for all UAS flight parameters, but the quality and quantity of extracted DBH values was maximized for lower altitude, nadir crosshatch acquisitions; 3) the distribution of predicted DBH values most closely matched field observed values for off-nadir crosshatch flight designs; 4) the use of either off-nadir or crosshatch flight designs at lower altitudes maximized precision and accuracy of stand density estimates.

2.4.1 Tree Location Extraction

Our best acquisitions for tree extraction accuracy and correctness (F-score = 0.77) is in the middle of extraction rates found for 30 sites using UAS-based singe tree detection (Mohan et al., 2017). However, our study includes all trees > 1.37 m tall whereas most studies only include dominant and codominant overstory trees, likely meaning our overstory extraction rate should be on the higher range of that reported in the literature. In comparison with a study conducted at the same study site, we saw 0.19 increase in F-score across all tree sizes with the only difference being the use of 0.10 cm CHM as opposed to a 0.25 cm CHM by Creasy et al. (*in review*). This suggests that CHM resolution should be further investigated to determine its impact on tree extraction rates.

Linear regression across the 30 UAS extracted tree datasets suggests some flexibility in flight parameters for maximizing F-score, precision, and recall (Table 2.1). UAS acquisitions conducted using a crosshatch flight pattern paired with nadir a camera angle maximized tree detection results (Figure 2.4). The indication of a nadir flight angle is counter to what has been seen in previous studies (Nesbit and Hugenholtz, 2019) that suggested 20-35° off-nadir imagery improves systematic SfM block bundle adjustment errors. We speculate that the consumer-grade GPS equipped in the DJI Phantom 4 Pro paired with the difficulty of identifying ground control points in off-nadir images led to greater miss-alignment errors compared to the nadir acquisitions. Further testing of off-nadir flight designs should explore using UAS platform with real time kinematic geolocation accuracy to reduce error through manual ground control point georegistration (Tomaštík et al., 2019).

2.4.2 UAS Extracted Height and DBH

The high extracted tree height correlations (r = >0.98) found in this study exceed what has previously been reported in ponderosa pine dominated forests (0.80-0.95; Belmonte et al., 2020). Our improved height correlations compared to Belmonte et al. (2020) may be attributed to their 15 cm resolution imagery as opposed to the finer resolution used in this study (1.8 and 3.2 cm at 65 and 115 m, respectively), with our finer resolution imagery likely capturing more canopy detail. Additionally, we had generally small tree height biases (< ±0.15 m) in all acquisitions, in line with, or slightly better than, accuracies reported in other UAS studies (e.g., -0.13 to -0.38 m; Krause et al., 2019).

This study's highest extracted tree DBH rates (> 40%) were achieved with crosshatch flight patterns using moderately off-nadir camera angles (25-30°) that provided more complete stem reconstruction (Figure 2.9). Previous work has demonstrated how the increased overlap of crosshatch flight designs improves image registration and provide increased point densities beneath the dominant forest canopy (Dandois et al., 2015; Seifert et al., 2019). However, even our best extraction rate (47.8%) falls below that of Fritz et al. (2013) who extracted 70% of DBH values using off-nadir UAS datasets in a leaf-off deciduous forest. Our lower extraction rates are likely due to occlusion caused by the persistent coniferous canopy, resulting in lower point densities within the DBH point cloud slices than was seen in Fritz et al. (2013). However, incomplete extraction of DBHs was expected, with the hope that enough DBH values would be available for UAS modeling of the missing DBH values.

Filtering of the extracted heights and DBHs that were spatially matched with the FIA regional height to DBH relationship removed a substantial component of falsely extracted DBH values. Despite extracting an average of 31.1% of DBHs, only 8.1% of DBH values on average were retained through the filtering process. In considering just overstory forest structure (tree > 6 tall), the best DBH extraction flight (65 m altitude; crosshatch; 25° camera angle) retained 20.5% of DBHs through the filtering process. Unfiltered extracted DBHs varied widely in their correlation (0.554-0.886) with field observed DBHs across the flight designs. However, the filtering process increased correlations to 0.871-0.920, with these tending to be strongest for crosshatch and off-nadir flight designs (Figure 2.6). These correlations exceed the 0.696 correlation achieved by Fritz et al. (2013) through direct DBH extraction but was in-line with the 0.911 reported in González-Jaramillo et al. (2019), who utilized a pre-existing local height to DBH relationship. This filtering process was able to remove erroneously extracted DBH values that likely resulted from partially reconstructed stems or branches within the point cloud slice, leaving an average of 72 UAS extracted DBHs in each dataset to generate a UAS-based height to DBH relationship.

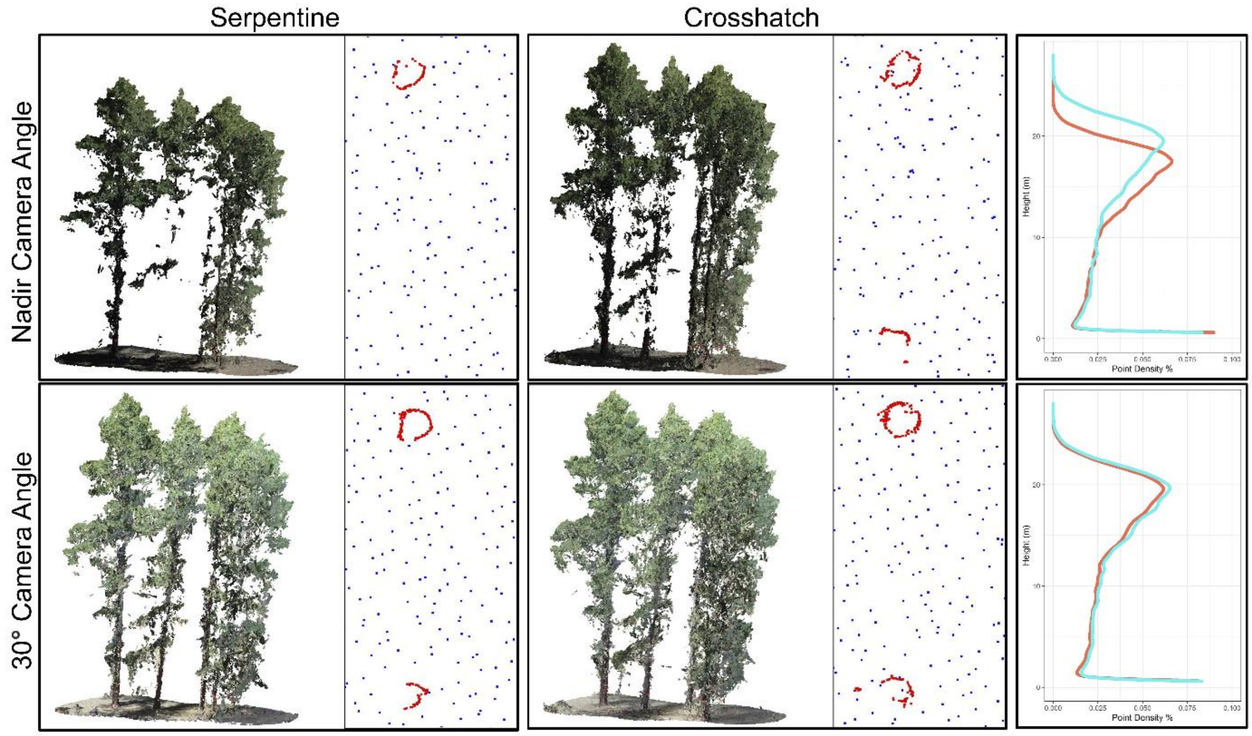

Figure 2.9. Visualization of serpentine (left) and crosshatch (middle) point clouds and DBH slices from 65 m acquisitions at nadir (top) and 30° off-nadir (bottom). Point cloud distributions (right) are shown for the serpentine (red) and crosshatch (blue) acquisitions at the same camera angles.

2.4.3 Local UAS height to DBH relationships

The filtered pairs of extracted tree heights and DBHs provided a large enough sample dataset to create UAS-based height to DBH relationships for estimating missing DBH values associated with each UAS extracted tree height. The UAS predicted DBH values tended to overestimate diameters for smaller trees and underestimated the largest diameters (Figure 2.7). Errors at the DBH distribution tails are somewhat expected as these values are less represented in the extracted data pairs and likely present unaccounted for variation in local growing environments. Particularly for smaller trees growing in dense environments or beneath the crowns of mature trees, they often allocate greater resources to height growth compared to DBH growth (Barret, 1982). This is at least partially supported by other studies that have found UAS estimates of crown diameter and area to improve predictions of DBH compared to height only models (Iizuka et al., 2018). Our local UAS-based modeling of DBH could be improved by exploring other UAS-based predictors in a multiple linear regression capable of accounting for density by including metrics like delineated crown area or extracted local stem density.

2.4.4 Estimations of Plot- and Stand-Level Metrics

Across all metrics of forest density (overstory and understory TPH and overstory basal area per hectare), the best performing acquisitions had plot-level correlations exceeding 0.8 with field observed density metrics. Of the tested UAS datasets, 40% had correlations exceeding 0.8 for overstory TPH (> 6 m tall) and field observed TPH, with the strongest correlations coming from crosshatch and off-nadir flight designs. However, acquisitions with a 35° camera angle had correlations < 0.5. Our strength in estimating overstory TPH aligns with previous studies (Bonnet et al., 2017), and indicate that the relative trend in overstory tree density was captured. However, the best performing models failed to identify two trees in each 0.04 ha plot on average, resulting in an underestimation bias of 13% or ~50 TPH.

Similar high correlations (>0.8) were found for estimates of understory TPH for all but the serpentine 35° off-nadir acquisitions. The best correlation values exceeded 0.9, with all of these being 65 m altitude acquisitions using either off-nadir or crosshatch flight designs. However, the underestimation bias of understory tree density was larger at an average of 4 trees per plot, equivalent to 20% or ~100 TPH at the stand level. This increased negative bias for understory trees aligns with the decreased probability of detecting understory trees using single tree detection strategies described in other studies (Creasy et al., *in review*).

Across the 30 UAS datasets, the four top correlations exceeded 0.8 for estimates of overstory basal area per acre and were acquired at 65 m altitude with either off-nadir or crosshatch flight designs. For these high correlation datasets plot-level basal area per hectare RMSE was 27-37%. However, when summarized at the stand scale 43% of datasets estimated overstory basal area per hectare to within 10% (2.3 m^2 ha^{-1}). This high accuracy at the stand level is similar to that reported by Belmonte et al. (2020) who evaluated basal area in pre- and post-treatment ponderosa pine. This indicates that while the relative trend and stand average basal area per hectare were accurately captured, within-stand variation was spatially misaligned. Visual inspection of plot-level basal area per hectare residuals showed that the largest error terms were spatially correlated in neighboring plots, such that large positive errors were next to large negative errors. The authors take this spatially correlation in errors to indicate that small location differences between extracted and stem mapped trees might explain the relatively large RMSE.

Ranking acquisitions based on having high plot-level correlations along with minimizing stand-level error for all density metrics places seven 65 m altitude acquisitions in the top 10 datasets, with this including all five crosshatch datasets. This suggests that individual tree assessment for describing plot- and stand-level forest structure in ponderosa pine systems is best described through lower altitude UAS flights using either off-nadir or crosshatch flight designs. Our high correlation and precision in modeling overstory forest structure has potential as a tool in guiding development of ponderosa pine silvicultural prescriptions that typically aim to increase horizontal and vertical forest heterogeneity.

2.4.5 Tree-Based UAS Monitoring Applications

The increased focus on spatial heterogeneity management objectives within dry conifer forests has elevated the need for monitoring strategies capable of describing the matrix of trees, groups of trees, and openings that comprise a stand (Tinkham et al., 2017). This study's demonstrated UAS individual tree extraction workflow could provide complete tree lists of locations, heights, and DBHs within low and moderate density (< 1000 TPH) conifer forest systems. Having spatially informed tree-level characteristics could enable silvicultural prescription development for a range of restoration, resilience, and wildlife focused objectives.

Such tree lists would be a valuable resource for land managers planning and implementing spatially explicit silvicultural prescriptions and would enable managers to map explicit locations for tree retention and planned openings for use by marking crews. Implementing matrices of openings and tree groups through dry conifer restoration has been found to limit crown fire spread (Beaty and Taylor, 2007) and reduce beetle mortality intensity by fragmenting continuity between susceptible hosts (Fettig et al., 2007). Such management strategies often target removal of understory and suppressed trees, and while our understory estimates do not reflect exact density levels, the results capture relative understory densities across the stand which could guide thinning objectives that target understory trees (Allen et al., 2002). While not all trees were successfully extracted from the UAS data, the presented methods capture both the relative local trends and stand-level averages that are necessary for informing a broad range of thinning and restoration actions in lower density forests (< ~1,000 tree ha^{-1}) like temperate and montane pine dominated systems.

Integration of multispectral information into these tree-level methods has potential to further extend the applications of UAS tree-based monitoring. Such tree-level characterization of species and structural distributions would be valuable for assessment and management of species-specific wildlife habitat and diversity patterns that are often correlated with vertical and horizontal forest structure (Merrick et al., 2013). Additionally, extending similar UAS techniques to monitor temporal change in habitat distributions for species of conservation interest (Vogeler et al., 2016) or assessing the outcomes of forest restoration activities (Almeida et al., 2019) would fulfill many adaptive management mandates.

While the presented UAS methods have potential to characterize stand wide tree lists of locations, heights, and DBHs, these approaches have only been tested at a small scale (1 ha). For such approaches to be fully operationalized in land management further testing needs to be conducted across a broader range of forest structure and species compositions. Further testing will help identify the range of forest conditions that UAS tree-based monitoring can be used to reliably inform management decisions.

2.5 Conclusions and Suggestions

This study demonstrates a novel UAS-based inventory strategy for estimating individual tree structural attributes (i.e., location, height, and DBH) in dry conifer forests. We found that a crosshatch flight pattern (1) maximized UAS SfM individual tree detection rates and (2) minimized extracted tree height and DBH errors. Additionally, we found that combining crosshatch with off-nadir camera angles (3) improved UAS-based modeling of individual tree

DBH and (4) provided the best representation of plot- and stand-level density metrics. Our filtering of UAS extracted DBH samples with national forest inventory data appears to provide a route for modeling individual tree DBH values, without the need for *in situ* field observations. Despite the high accuracy of modeled stand basal area estimates, accuracy of individual tree DBHs increased for both the smallest and largest trees. Future work should explore how other UAS derived attributes like stem density, crown area, and relative height compared to neighboring trees could account for competition impacts on modeled individual tree DBHs. The spatial tree list of heights and DBHs provided by this study's UAS individual tree extraction workflow could provide the tree-level characteristics needed for silvicultural prescription development for a range of restoration, resilience, and wildlife focused objectives.

Operationalizing UAS-based individual tree inventories will require balancing data precision against characterizing broader extents (10s–100s ha). The crosshatch data acquisition conducted in this study doubled the data acquisition time, image storage requirements, and processing time to gain an estimated 5-10% improvement in UAS derived inventory products. The largest benefit of the crosshatch flight pattern came from an ~30% increase in the number of DBH values successfully extracted and matched with UAS derived tree heights compared to the serpentine pattern. However, the results make it clear that it is unrealistic to expect above canopy UAS acquisitions to capture all DBH values. Meaning UAS-based individual tree inventories might see efficiency gains by flying entire stands with serpentine patterns and then sample portions of a stand with a crosshatch pattern to improve DBH extraction rates. Work is needed to understand what proportion of a stand needs to be sampled with the crosshatch pattern to ensure enough DBH values are extracted to impute the missing DBH values.

Cited Works

Addington, R.N., Aplet, G.H., Battaglia, M.A., Briggs, J.S., Brown, P.M., Cheng, A.S., Dickinson, Y.A., Feinstein, J.A., Pelz, K.A., Regan, C.M., Thinnes, J.W., Truex, R.L., Fornwalt, P.J., Gannon, B., Julian, C.W., Underhill, J.L., & Wolk, B. 2018. Principles and practices for the restoration of ponderosa pine and dry mixed-conifer forests of the Colorado Front Range. Gen. Tech. Rep. RMRS-GTR-373. Fort Collins, CO: U.S. Department of Agriculture, Forest Service, Rocky Mountain Research Station. 121 p.

Allen, C. D., Savage, M., Falk, D.A., Suckling, K.F., Swetnam, T.W., Schulke, T., Stacey, P.B., Morgan, P., Hoffman, M., & Klingel, J.T. 2002. Ecological Restoration Of Southwestern Ponderosa Pine Ecosystems: A Broad Perspective. Ecological Applications, 12(5), 1418–1433, doi: 10.1890/1051-0761(2002)012[1418:erospp]2.0.co;2.

Almeida, D.R.A., Broadbent, E.N., Zambrano, A.M.A., Wilkinson, B.E., Ferreira, M.E., Chazdon, R., Meli, P., Gorgens, E.B., Silva, C.A., Stark, S.C., & Valbuena, R. 2019. Monitoring the structure of forest restoration plantations with a drone-lidar system. International Journal of Applied Earth Observation and Geoinformation, 79: 192-198.

Battaglia, M.A., Gannon, B., Brown, P.M., Fornwalt, P.J., Cheng, A.S., & Huckaby, L.S. 2018. Changes in forest structure since 1860 in ponderosa pine dominated forests in the Colorado and Wyoming Front Range, UAS. Forest Ecology and Management, 422, 147-160, doi: 10.1016/j.foreco.2018.04.010.

Barrett, J.W. 1982. Twenty-Year Growth of Ponderosa Pine Saplings Thinned to Five Spacings in Central Oregon. Pacific Northwest Forest and Range Experiment Station, U.S. Dept. of Agriculture, Forest Service, DOI.org (Crossref), doi:10.5962/bhl.title.88007.

Beaty, R. M., & Taylor, A. H. 2007. Fire disturbance and forest structure in old-growth mixed conifer forests in the northern Sierra Nevada, California. Journal of Vegetation Science, 18(6), 879–890. doi: 10.1111/j.1654-1103.2007.tb02604.x.

Belmonte, A., Sankey, T., Biederman, J.A., Bradford, J., Goetz, S.J., Kolb, T., & Woolley, T. 2020. UAV-derived estimates of forest structure to inform ponderosa pine forest restoration. Remote Sensing in Ecology and Conservation, doi: 10.1002/rse2.137.

Bonnet, S., Lisein, J., & Lejeune, P. 2017. Comparison of UAS photogrammetric products for tree detection and characterization of coniferous stands. International Journal of Remote Sensing, 38(19), 5310–5337, doi: 10.1080/01431161.2017.1338839.

Boyden, S., Binkley, D., & Shepherd, W. 2005. Spatial and temporal patterns in structure, regeneration, and mortality of an old-growth ponderosa pine forest in the Colorado Front Range. Forest Ecology and Management, 219(1), 43-55.

Cannon, J.B., Barrett, K.J., Gannon, B.M., Addington, R.N., Battaglia, M.A., Fornwalt, P.J., Aplet, G.H., Cheng, A.S., Underhill, J.L., Briggs, J.S., & Brown, P.M. 2018. Collaborative restoration effects on forest structure in ponderosa pine-dominated forests of Colorado. Forest Ecology and Management, 424, 191–204, doi: 10.1016/j.foreco.2018.04.026.

Cook, K.L. 2017. An evaluation of the effectiveness of low-cost UAVs and structure from motion for geomorphic change detection. Geomorphology, 278, 195–208, doi: 10.1016/j.geomorph.2016.11.009

Conto, T. 2019. TreeLS: Terrestrial Point Cloud Processing of Forest Data. R package version 1.0. https://CRAN.R-project.org/package=TreeLS

Conto, T.D., Olofsson, K., Görgens, E.B., Rodriguez, L.C.E., & Almeida, G. 2017. Performance of stem denoising and stem modelling algorithms on single tree point clouds from terrestrial laser scanning. Computers and Electronics in Agriculture, 143, 165–176, doi: 10.1016/j.compag.2017.10.019.

Creasy, M.B., Tinkham, W.T., Hoffman, C.M., & Vogeler, J.C. Potential for individual tree Monitoring in ponderosa pine-dominated forests using unmanned aerial system structure from motion point clouds. Canadian Journal of Forest Research, IN REVIEW.

Dandois, J.P. & Ellis, E.C. 2013. High spatial resolution three-dimensional mapping of vegetation spectral dynamics using computer vision. Remote Sensing of Environment, 136, 259–276, doi: 10.1016/j.rse.2013.04.005.

Dandois, J., Olano, M., & Ellis, E. 2015. Optimal Altitude, Overlap, and Weather Conditions for Computer Vision UAV Estimates of Forest Structure. Remote Sensing, 7(10), 13895–13920, doi: 10.3390/rs71013895.

Díaz, G.M., Mohr-Bell, D., Garrett, M., Muñoz, L., & Lencinas, J.D. 2020. Customizing unmanned aircraft systems to reduce forest inventory costs: can oblique images substantially improve the 3D reconstruction of the canopy? International Journal of Remote Sensing, 41(9), 3480–3510, doi: 10.1080/01431161.2019.1706200.

Dixon, G.E. 2002. Essential FVS: A user’s guide to the Forest Vegetation Simulator. USDA Forest Service, Internal Report, Forest Management Service Center, 204 p.

Falkowski, M.J., A.M.S. Smith, A.T. Hudak, P.E. Gessler, L.A. Vierling and N.L. Crookston. 2006. Automated estimation of individual conifer tree height and crown diameter via two-dimensional spatial wavelet analysis of lidar data. *Canadian Journal of Remote Sensing* 32: 153-161.

Fettig, C. J., Klepzig, K. D., Billings, R. F., Munson, A. S., Nebeker, T. E., Negrón, J. F., & Nowak, J. T. 2007. The effectiveness of vegetation management practices for prevention and control of bark beetle infestations in coniferous forests of the western and southern United States. Forest Ecology and Management, 238(1-3), 24–53. doi: 10.1016/j.foreco.2006.10.011.

Forsman, M., Börlin, N., & Holmgren, J. 2016. Estimation of Tree Stem Attributes Using Terrestrial Photogrammetry with a Camera Rig. Forests, 7(12), 61, doi: 10.3390/f7030061.

Frey, J., Kovach, K., Stemmler, S., and Koch, B. 2018. UAV Photogrammetry of Forests as a Vulnerable Process. A Sensitivity Analysis for a Structure from Motion RGB-Image Pipeline. Journal of Remote Sensing, 10(6): 912, doi: 10.3390/rs10060912.

Fritz, A., Kattenhorn, T., & Koch, B. 2013. UAV-based photogrammetric point clouds - tree stem mapping in open stands in comparison to terrestrial laser scanner point clouds. International Archives of the Photogrammetry, Remote Sensing and Spatial Information Sciences, XL-1: W2, doi: 10.5194/isprsarchives-XL-1-W2-141-2013.

González-Jaramillo, V., Fries, A., & Bendix, J. 2019. AGB estimation in a tropical mountain forest (TMF) by means of RGB and multispectral images using an unmanned aerial vehicle (UAV). Remote Sensing, 11(12), 1413, doi: 10.3390/rs11121413.

Heinzel, J. & Huber, M. 2016. Detecting Tree Stems from Volumetric TLS Data in Forest Environments with Rich Understory. Remote Sensing, 9(1), 9, doi: 10.3390/rs9010009.

Hopkinson, C., Chasmer, L., Young-Pow, C., & Treitz, P. 2004. Assessing forest metrics with a ground-based scanning lidar. Canadian Journal of Forest Research, 34(3), 573–583, doi: 10.1139/x03-225.

Iizuka, K., Yonehara, T., Itoh, M., & Kosugi, Y. 2018. Estimating Tree Height and Diameter at Breast Height (DBH) from Digital Surface Models and Orthophotos Obtained with an Unmanned Aerial System for a Japanese Cypress (Chamaecyparis obtusa) Forest. Remote Sensing, 10(1), 13, doi: 10.3390/rs10010013.

Kandare, K., Ørka, H.O., Chan, J.C.-W., & Dalponte, M. 2016. Effects of forest structure and airborne laser scanning point cloud density on 3D delineation of individual tree crowns. European Journal of Remote Sensing, 49(1), 337–359, doi: 10.5721/eujrs20164919.

Krause, S., Sanders, T. G., Mund, J.-P., & Greve, K. 2019. UAV-Based Photogrammetric Tree Height Measurement for Intensive Forest Monitoring. Remote Sensing, 11(7), 758, doi: 10.3390/rs11070758.

Liang, X., Jaakkola, A., Wang, Y., Hyyppä, J., Honkavaara, E., Liu, J., & Kaartinen, H. 2014. The Use of a Hand-Held Camera for Individual Tree 3D Mapping in Forest Sample Plots. Remote Sensing, 6(7), 6587–6603, doi: 10.3390/rs6076587.

Maas, H.G., Bienert, A., Scheller, S., & Keane, E. 2008. Automatic forest inventory parameter determination from terrestrial laser scanner data. International Journal of Remote Sensing, 29(5), 1579–1593, doi: 10.1080/01431160701736406.

Merrick, M.J., Koprowski, J.L., & Wilcox, C. 2013. Into the third dimension: benefits of incorporating LiDAR data in wildlife habitat models. In: Gottfried, Gerald J.; Ffolliott, Peter F.; Gebow, Brooke S.; Eskew, Lane G.; Collins, Loa C. Merging science and management in a rapidly changing world: Biodiversity and management of the Madrean Archipelago III and 7th Conference on Research and Resource Management in the Southwestern Deserts; 2012 May 1-5; Tucson, AZ. Proceedings. RMRS-P-67. Fort Collins, CO: US Department of Agriculture, Forest Service, Rocky Mountain Research Station. p. 389-395. (Vol. 67, pp. 389-395).

Mikita, T., Janata, P., & Surový, P. 2016. Forest Stand Inventory Based on Combined Aerial and Terrestrial Close-Range Photogrammetry. Forests, 7(8), 165, doi: 10.3390/f7080165.

Mohan, M., Silva, C., Klauberg, C., Jat, P., Catts, G., Cardil, A., Hudak, A., & Dia, M. 2017. Individual Tree Detection from Unmanned Aerial Vehicle (UAV) Derived Canopy Height Model in an Open Canopy Mixed Conifer Forest. Forests, 8(9), 340, doi: 10.3390/f8090340.

Mokroš, M., Liang, X., Surový, P., Valent, P., Čerňava, J., Chudý, F., Tunák, D., Saloň, Š., & Merganič, J. 2018. Evaluation of Close-Range Photogrammetry Image Collection Methods for Estimating Tree Diameters. ISPRS International Journal of Geo-Information, 7(3), 93, doi: 10.3390/ijgi7030093.

Nesbit, P. & Hugenholtz, C. 2019. Enhancing UAV–SfM 3D Model Accuracy in High-Relief Landscapes by Incorporating Oblique Images. Remote Sensing, 11(3), 239, doi: 10.3390/rs11030239.

Nilsson, M. 1996. Estimation of tree heights and stand volume using an airborne lidar system. Remote Sensing of Environment, 56(1), 1–7, doi: 10.1016/0034-4257(95)00224-3.

North, M., Stine, P., O'Hara, K., Zielinski, W., & Stephens, S. 2009. An ecosystem management strategy for Sierra mixed-conifer forests. Gen. Tech. Rep. PSW-GTR-220. Albany, CA: U.S. Department of Agriculture, Forest Service, Pacific Southwest Research Station. 49 p.

Paris, C., Kelbe, D., Aardt, J.V., & Bruzzone, L. 2017. A Novel Automatic Method for the Fusion of ALS and TLS LiDAR Data for Robust Assessment of Tree Crown Structure. IEEE Transactions on Geoscience and Remote Sensing, 55(7), 3679–3693, doi: 10.1109/tgrs.2017.2675963.

Piermattei, L., Karel, W., Wang, D., Wieser, M., Mokroš, M., Surový, P., Koreň, M., Tomaštík, J., Pfeifer, N., Hollaus, M. 2019. Terrestrial Structure from Motion Photogrammetry for Deriving Forest Inventory Data. Remote Sensing, 11(8), 950, doi: 10.3390/rs11080950.

Pinheiro, J., Bates, D., DebRoy, S., & Sarkar, D. 2018. nlme: Linear and Nonlinear Mixed Effects Models. R package version 3.1-137, https://CRAN.R-project.org/package=nlme

Plowright, A. 2018. ForestTools: Analyzing Remotely Sensed Forest Data. R package version 0.2.0. https://CRAN.R-project.org/package=ForestTools

Popescu, S.C. & Wynne, R.H. 2004. Seeing the Trees in the Forest. Photogrammetric Engineering & Remote Sensing, 70(5), 589–604, doi: 10.14358/pers.70.5.589.

R Core Team. 2019. R: A language and environment for statistical computing. R Foundation for Statistical Computing, Vienna, Austria.

Roussel, J.R. & Auty, D. 2019. lidR: airborne LiDAR data manipulation and visualization for forestry applications. R package version 2.0.2. https://CRAN.R-project.org/package=lidR

Reynolds, R.T., Meador, A.J.S., Youtz, J.A., Nicolet, T., Matonis, M.S., Jackson, P.L., DeLorenzo, D.G., & Graves, A.D. 2013. Restoring composition and structure in Southwestern frequent-fire forests: A science-based framework for improving ecosystem resiliency. Gen. Tech. Rep. RMRS-GTR-310. Fort Collins, CO: U.S. Department of Agriculture, Forest Service, Rocky Mountain Research Station. 76 p.

Saarinen, N., Kankare, V., Vastaranta, M., Luoma, V., Pyörälä, J., Tanhuanpää, T., Liang, X., Kaartinen, H., Kukko, A., Jaakkola, A., Yu, Xiaowei., Holopainen, M., & Hyyppä, J. 2017. Feasibility of Terrestrial laser scanning for collecting stem volume information from single trees. ISPRS Journal of Photogrammetry and Remote Sensing, 123, 140–158, doi: 10.1016/j.isprsjprs.2016.11.012.

Sačkov, I., Kulla, L., & Bucha, T. 2019. A Comparison of Two Tree Detection Methods for Estimation of Forest Stand and Ecological Variables from Airborne LiDAR Data in Central European Forests. Remote Sensing, 11(12), 1431, doi: 10.3390/rs11121431.

Seifert, E., Seifert, S., Vogt, H., Drew, D., Aardt, J. V., Kunneke, A., and Seifert, T. 2019. Influence of Drone Altitude, Image Overlap, and Optical Sensor Resolution on Multi-View Reconstruction of Forest Images. Remote Sensing, 11(10): 1252, doi: 10.3390/rs11101252

Silva, C.A., Hudak, A.T., Vierling, L.A., Loudermilk, E.L., O'Brien, J.J., Hiers, J.K., Jack, S.B., Gonzalez-Benecke, C., Lee, H., Falkowski, J.M., & Khosravipour, A. 2016. Imputation of Individual Longleaf Pine (Pinus palustrisMill.) Tree Attributes from Field and LiDAR Data. Canadian Journal of Remote Sensing, 42(5), 554–573, doi: 10.1080/07038992.2016.1196582.

Swayze, N., Creasy, M., Tinkham, W., Vogeler, J., Hudak, A., Hoffman, C., *in prep*. Influence of UAS flight altitude and speed on aboveground biomass modeling. For submission to Drones.

Tinkham, W.T., Dickinson, Y., Hoffman, C.M., Battaglia, M.A., Ex, S., & Underhill, J. 2017. Visualization of heterogeneous forest structures following treatment in the southern Rocky Mountains. Gen. Tech. Rep. RMRS-GTR-365. Fort Collins, CO: U.S. Department of Agriculture, Forest Service, Rocky Mountain Research Station, 72 p., doi:

Tinkham, W.T., Mahoney, P.R., Hudak, A.T., Domke, G.M., Falkowski, M.J., Woodall, C.W., & Smith, A.M.S. 2018. Applications of the United States Forest Inventory and Analysis dataset: a review and future directions. Canadian Journal of Forest Research, 48(11), 1251-1268, doi: 10.1139/cjfr-2018-0196.

Tinkham, W.T., Smith, A.M.S., Affleck, D.L.R., Saralecos, J.D., Falkowski, M.J., Hoffman, C.M., Hudak, A.T., and Wulder, M.A. 2016. Development of height-volume relationships in second growth Abies grandis for use with aerial LiDAR. Canadian Journal of Remote Sensing, 42(5): 400-410, doi: 10.1080/07038992.2016.1232587.

Thiel, C. & Schmullius, C. 2016. Comparison of UAV Photograph-Based and Airborne Lidar-Based Point Clouds over Forest from a Forestry Application Perspective. International Journal of Remote Sensing, 38(8-10): 2411-2426, doi:10.1080/01431161.2016.1225181.

Tomaštík, J., Mokroš, M., Surový, P., Grznárová, A., & Merganič, J. 2019. UAV RTK/PPK Method—An Optimal Solution for Mapping Inaccessible Forested Areas? Remote Sensing, 11(6), 721, doi: 10.3390/rs11060721.

Venables, W.N. & Ripley, B.D. 2002. Modern applied statistics with S. Fourth Edition. Springer, New York, New York, UAS. ISBN 0-387-95457-0.

Vogeler, J.C., Yang, Z., & Cohen, W.B. 2016. Mapping Suitable Lewis's Woodpecker Nesting Habitat in a Post-Fire Landscape. Northwest Sci., 90(4), 421-432.

You, L., Tang, S., Song, X., Lei, Y., Zang, H., Lou, M., & Zhuang, C. 2016. Precise Measurement of Stem Diameter by Simulating the Path of Diameter Tape from Terrestrial Laser Scanning Data. Remote Sensing, 8(9), 717, doi: 10.3390/rs8090717.

Wilkes, P., Jones, S.D., Suarez, L., Haywood, A., Mellor, A., Woodgate, W., Soto-Berelov, M., & Skidmore, A.K. 2015. Using discrete-return airborne laser scanning to quantify number of canopy strata across diverse forest types. Methods in Ecology and Evolution, 7(6), 700–712, doi: 10.1111/2041-210x.12510.

Ziegler, J., Hoffman, C., Fornwalt, P., Sieg, C., Battaglia, M., Chambers, M., & Iniguez, J. 2017. Tree Regeneration Spatial Patterns in Ponderosa Pine Forests Following Stand-Replacing Fire: Influence of Topography and Neighbors. Forests, 8(10), 391, doi: 10.3390/f8100391.

Appendix

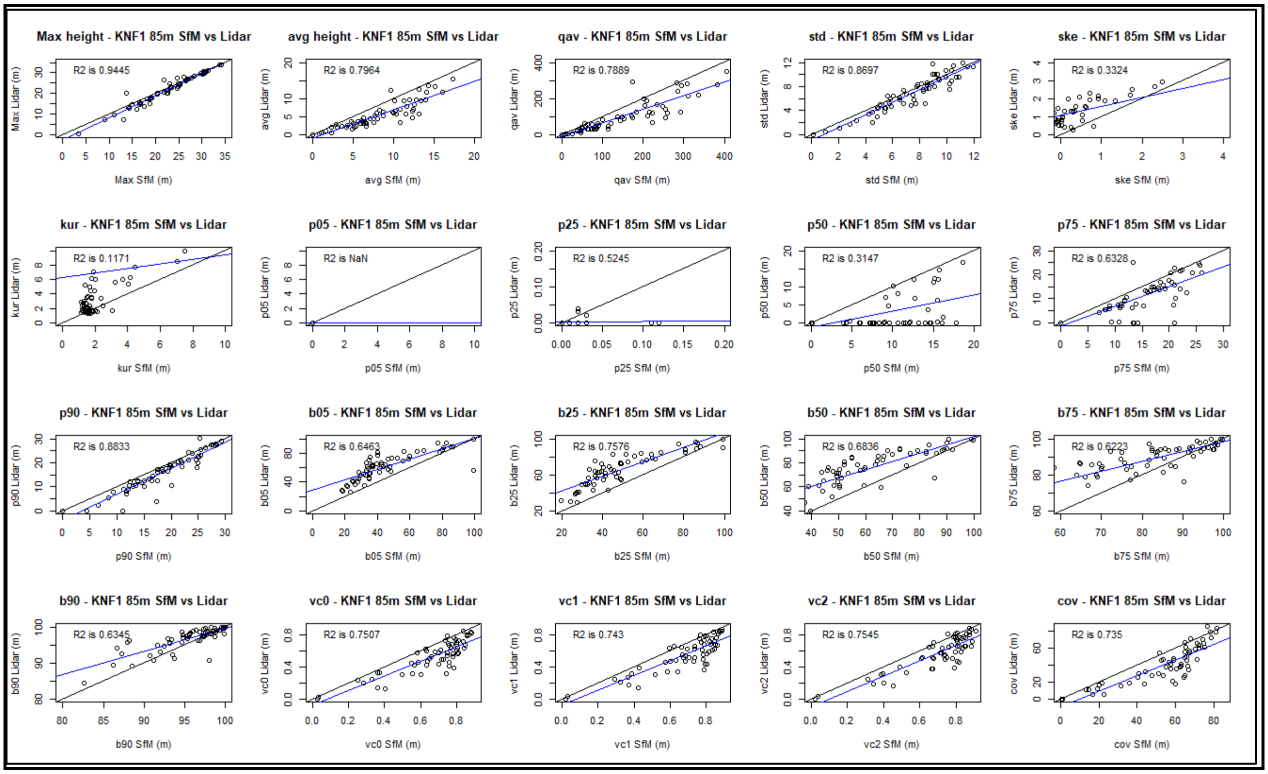

Supplemental Figure 1.1: LiDAR vs SfM point cloud structural metric comparisons for the model with the highest improved variance compared to LiDAR, which was the 85 m AGL altitude at KNF1, which had an improved variance of 26.3% over the LiDAR AGB model for that site.

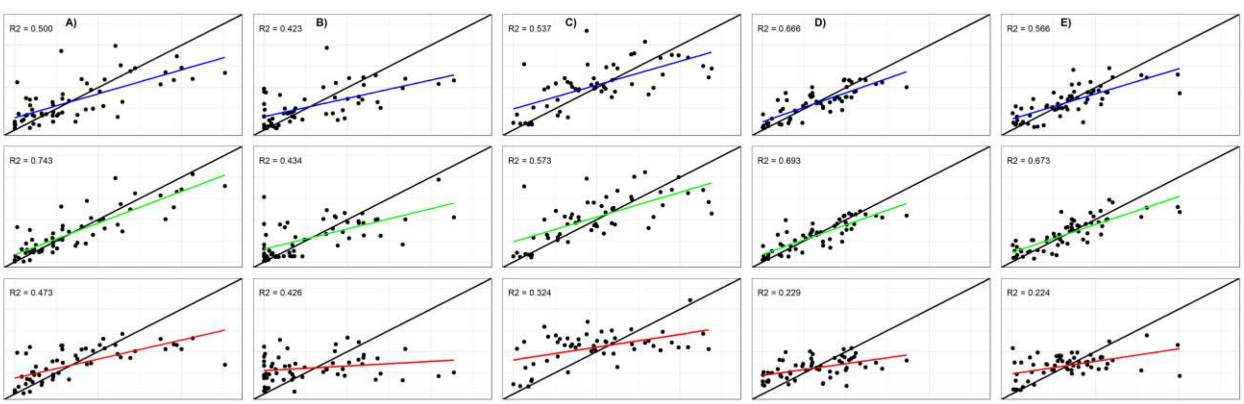

Supplemental Figure 1.2: Observed (x axis) vs Predicted (y axis) for KNF1 (A), KNF2 (B), KNF3 (C), MEF1 (D), and MEF2 (E) AGB models, representing from top to bottom the LiDAR (blue line), highest altitude UAS (green line), and lowest altitude UAS (red line) models for each study area.

Supplemental Table 1.1. Agisoft Metashape processing parameters for SfM photogrammetry forest reconstruction.

Parameter	Setting
Align Photos	
Accuracy	Highest
Generic preselection	Yes
Reference preselection	Source
Reset current alignment	No
Key point limit	40,000
Tie Point Limit	4000
Apply masks to	None
Adaptive camera model fitting	Yes
Optimize Alignment	
Adaptive camera model fitting	Yes
Build Dense Cloud	
Quality	High
Depth Filtering	Mild
Calculate point colors	Yes
Calculate point confidence	No

Supplemental Table 2.1. Detailed settings for Altizure and Pix4D Capture automated flight applications.

Altizure	Pix4d
Focus: set to infinity	White balance: Auto
ISO: 100	Picture trigger mode: fast
Aperture: f5.6	Look at grids center (no)
Shutter Speed: 1/500th of second	
Min timed shot interval: 2 seconds	

Supplemental Table 2.2. Full suite of flight altitude, camera angle, and survey type image dataset combinations.

Flight Altitude (m)	Traditional (serpentine pattern)	Crosshatch (double serpentine pattern)
65	0°, 20°, 25°, 30°, 35°	0°, 20°, 25°, 30°, 35°
90	0°, 20°, 25°, 30°, 35°	0°, 20°, 25°, 30°, 35°
115	0°, 20°, 25°, 30°, 35°	0°, 20°, 25°, 30°, 35°